UNIVERSITY OF CALIFORNIA
RIVERSIDE

# An STM Study of Molecular Self-Assemblies on Cu(111): Structure, Interaction, and Effects of Confinement

A Dissertation submitted in partial satisfaction
of the requirements for the degree of

Doctor of Philosophy

in

Chemistry

by

Miaomiao Luo

June 2012

Dissertation Committee:
Dr. Ludwig Bartels, Chairperson
Dr. Jingsong Zhang
Dr. Gregory Beran

The Dissertation of Miaomiao Luo is approved:

_____

_____

_____

Committee Chairperson

University of California, Riverside

# ACKNOWLEDGEMENTS

I lack words, with which to express my thanks to my advisor Dr. Ludwig Bartels, for the opportunity he offered me to learn and conduct research in this wonderful group at UCR, for the sagacious guidance in all the fascinating adventures of exploring uncharted areas of surface science, for the considerate and thoughtful advices and help on my study and future career, and for setting a great model of a knowledgeable and brilliant scientist.

Also, the works included in this dissertation couldn't have been accomplished without the help of my group mates (current and former), Dr. Zhihai Cheng, Dr. Dezheng Sun, Dr. Daeho Kim, Wenhao Lu, Yeming Zhu, who helped me with the experimental measurements; and Jon Wyrick, Kamelia Cohen, Eric Chu, Connor Holzke, Daniel Salib, for their theoretical support.

I'd like to send my special thanks to my lab mate Sarah Bobek, who not only helped me on the experimental measurements, but also went through the big headache of reading through my dissertation and correcting grammar mistakes.

And thanks to the members left, John Mann, Quan Ma, Chen Wang, and KatieMarie Magnone, for keeping such a pleasant atmosphere in our lab.

Appreciation should also be given to every living creature with a good conscience, who is wishing, praying, and acting for a better world.

ABSTRACT OF THE DISSERTATION

An STM Study of Molecular Self-Assemblies on Cu(111):
Structure, Interaction, and Effects of Confinement

by

Miaomiao Luo

Doctor of Philosophy, Graduate Program in Chemistry
University of California, Riverside, June 2012
Dr. Ludwig Bartels, Chairperson

The self-assembly of several molecular species on Cu(111) has been studied with ultra-high vacuum scanning tunneling microscopy on the structures, interactions, and confinement effects. A coexistence of small flower and interlocking pinwheel structure is observed for the self-assembly of phenyl-propynenitrile molecules, with the preference of the more complex pinwheel structure attributed to the surface stress induced by molecular adsorption. Metal-organic coordination interaction on a 2-dimensional surface has been explored through a comparative study of isocyanide and cyanide molecules with the same molecular backbones. And the effect of confinement into self-assembled anthraquinone cavities has been demonstrated.

# Table of Contents

# List of Figures

# 1 Introduction

Organic molecules are found to autonomously assemble into particular arrangements on atomically flat surfaces without external guidance (Fig.1.1). This attracted a lot of interest in the past few decades, since it makes up an important sector of the bottom-up fabrication route in nanotechnology. The molecular self-assembly provides a means of patterning surfaces that can reach a smaller scale (~nanometers)[1] than which the conventional top-down methods, such as lithographic techniques, are fundamentally limited due to diffraction. An additional advantage is the parallel processing capability that allows much higher efficiency, compared to the conventional serial fabrication[2].

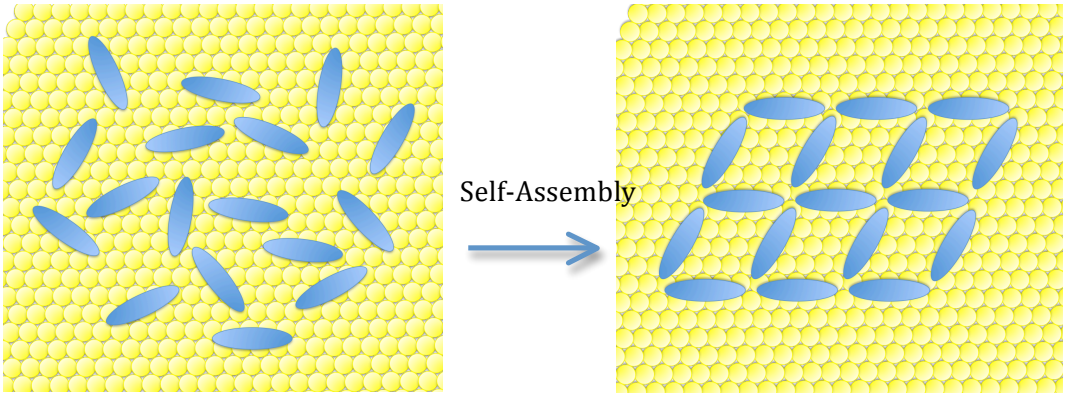


**Fig. 1.1** Schematic of autonomous molecular self-assembly on an atomically flat surface.

The networks formed through molecular self-assembly open the door for investigation in domains of nanoscience other than just the tailoring surfaces. The

cavities within the networks can serve as templates to stabilize subsequently deposited molecules[3-5]. They also allow the possibility of studying molecular behaviors such as diffusion[6], selective adsorption, etc., as well as surface states[6,7] trapped in nano-scale confinements with a uniform size. Catalytic properties can be activated for the unsaturated bond of the adsorbates[8]. In addition, guiding molecules into highly ordered structures with tunable sizes in a controlled manner[9,10] also sheds new light on concepts for fabricating nanodevices from the molecular level[11,12].

There have been many studies on self-assemblies with different molecular (and atomic) building blocks. Various networks arise with the cavity sizes ranging from sub-nm to ~10nm range[13], and shapes from rectangles[10,14] and hexagons[9,13,15,16] to pinwheels[17] and stars[18].

On the other hand, there is still much work to be done to fully understand the molecule/substrate system. A more complete understanding of the interactions within different molecule-substrate systems, as well as various novel properties found in different molecular self-assemblies is necessary.

## 1.1 Molecules at Metal Surfaces

Many types of substrates have been investigated, including metals (e.g. Cu, Ag, Au, Pd, etc.), oxides (e.g. $TiO_2$), silicon and graphite surfaces. And they have been studied in various conditions, under vacuum/solid, liquid/solid, etc. The system of

molecules on metal surfaces under ultra-high vacuum (UHV) conditions will be briefly introduced in this section.

### 1.1.1 Metal Surfaces

The surface of a single crystal metal is different from a 2D cross-section of the bulk phase in both interlayer distances and periodicity of the atomic arrangement. Clean metal surfaces usually exhibit a contraction of the interlayer distance between the 1$^{st}$ and the 2$^{nd}$ layers of the surface atoms, as well as a compensating expansion between the 2$^{nd}$ and 3$^{rd}$ layers. Additionally, a reconstruction of the surface is also observed for many metal surfaces, such as Ir, Pt, and Au, during which process the forces in the surfaces are relaxed by rearranging the topmost layer of atoms away from their equilibrium positions in the bulk. The reconstruction can also be induced by the adsorption of molecules. There are steps and kinks on the surface, as well as adatoms "evaporating" from the step edges of the surface (depending on the temperature of the metal) distinguishing the surface rather than the bulk.[19]

### 1.1.2 Adsorption and Motions of Molecules

When an adsorbate lands on the surface, the molecule can sense the atomic arrangement of the surface with its functional groups, and bond to specific lattice sites. Some flexible molecules may adapt their intra-molecular degrees of freedom to optimize molecule-substrate interactions. Chirality can also be induced by confinement in 2D.[11]

Molecules can vibrate, rotate or diffuse on the surface[20-22]. Motions of rotation and diffusion of molecules can be excited by photons or by thermal activation, allowing molecules to overcome the potential barrier between different adsorption orientations or bonding sites. Substrates with symmetrical features can influence the molecules' movement along specific orientation or direction.

## 1.2 Interactions in Molecular Self-Assemblies

To control the pattern formation and exploit the unique properties of molecular self-assembly on surfaces, it is crucial to understand the interactions involved in the molecule-surface system. The interactions can be direct interactions between molecules such as hydrogen bonding, metal-ligand interaction, or substrate-mediated interactions that involve surface state electrons or surface reconstruction[12,23]. The assembled structure and functionality of the system can be a result of an intricate interplay of several of them. Some common interactions in molecule/metal substrate systems will be briefly introduced in the following section, which are cited from publication *Tailoring molecular layers at metal surfaces* (Nature Chemistry 2010) by L. Bartels.

### 1.2.1 Direct Intra-Molecular Interactions

The direct interaction between molecules can be hydrogen bonding, metal-ligand coordination interaction, covalent bonding, dipole-dipole interaction, Van der Waals interaction, etc. (Fig. 1.2)

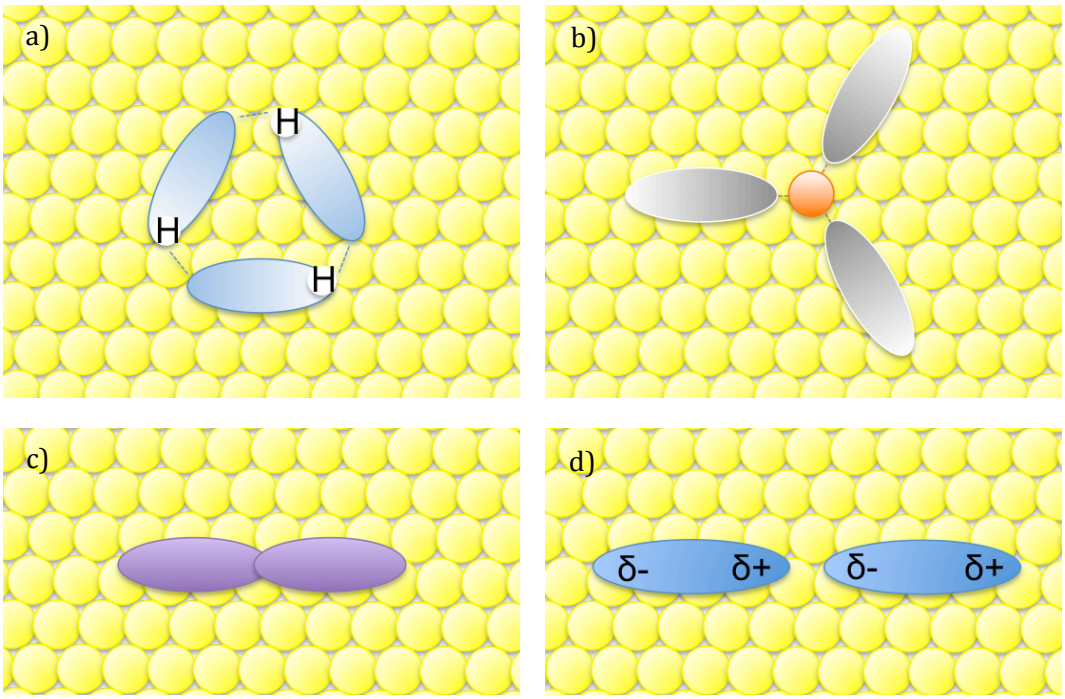


**Fig. 1.2** Direct intermolecular interactions on 2-dimensional surfaces. (a) Hydrogen bond, (b) Metal-ligand coordination interaction between metal adatoms and organic molecules, (c) Covalent bond, and (d) Dipole-dipole interactions

Hydrogen bonding is usually found between specific functional groups or atoms (e.g., carboxyl groups, cyano groups, sulfur atoms, etc.) and H atoms in the molecular building blocks, with a bond energy at ~0.05-0.7eV range, and bond length ~1.5-3.5Å[11,15,24]. Hydrogen bonding is reversible and directional, which enables rational design of supramolecular structures through self-assembly.

Metal-ligand coordination interaction on surfaces has been reported in recent years, and it is found to have a charge-transfer phenomenon between metal adatoms and ligand moieties of organic molecules. Similar with hydrogen bonding,

the metal-ligand interaction is also functional group specific, directional and reversible. A difference is that the metal-ligand interactions have a higher bonding energy (~0.5-2eV[11]), which makes the metal-ligand coordination network more robust. Notably, metal adatoms dispersed in the network can also bring catalytic and magnetic properties[2,25,26].

The dipole-dipole interaction involve the electrostatic attraction between the polar moieties of molecules. Van der Waals interaction are weaker (binding energy ~0.02-0.1eV[11]), and usually do not manifest themselves clearly except between bulky chain-like branches. Covalent bond between adsorbates has the highest binding energy, yet it is irreversible once formed.

### 1.2.2 The Role of Substrate

Other than providing a 2D confinement, the metal substrate is playing an important role in guiding the molecules to form novel structures.

The substrate can direct the molecular building blocks to self-assemble into a structure with in the registry of the substrate lattice. The same species of molecules (and atoms) may self-assemble into different structures at substrates of different lattice symmetry, as indicated in Fig. 1.3. And experimental results on trimesic acid (TMA) molecules clearly show that TMA form linear-chain structures on Cu(110)[27] but clover-leaf structures on Cu(100)[28].

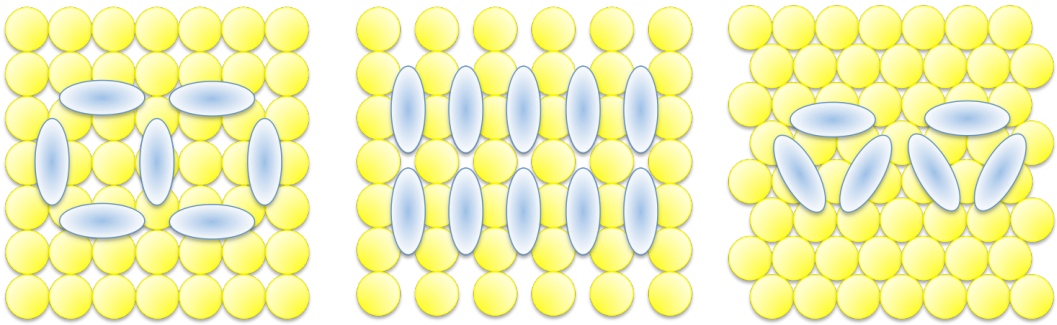

fcc(100) fcc(110) fcc(111)

**Fig. 1.3** The influence of substrate symmetry on the structure of molecular self-assembly. Molecules may assemble into different patterns to comply with the local registry of surfaces. In many cases, however, the symmetry feature of the substrate does not determine the structure of molecular self-assembly, especially when strong direct inter-molecular interactions play a role.

The substrate can also mediate lateral interaction between molecules through surface state electrons[23,29], or by releasing stress/strain induced by the adsorption of molecules[17,30]. (Fig. 1.4) The substrate-mediated interaction can be the crucial in forming regular supramolecular structures when inter-molecular interactions are relatively weak. This type of interaction can extend a much longer distance (~10Å range)[23] compared to the direct interactions between molecules, influencing the molecular assembly on a larger scale.

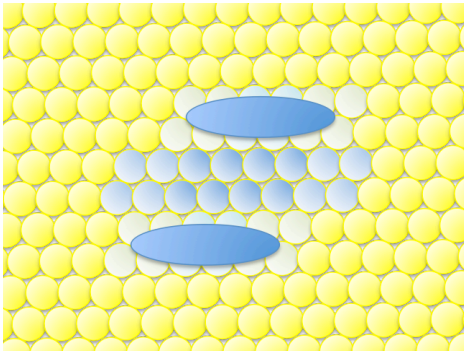

**Fig. 1.4** Substrate-mediated interactions on metal surfaces, including interactions mediated through surface state electrons, or surface strain/stress relief.

The above is a simplified description of the molecular self-assembly and interactions on metal surfaces. However, it serves as a baseline from which a more detailed discussion of surface activity can begin. A great deal of mechanistic details and novel properties are still waiting to be explored. This work represents a fundamental study of many such reaction mechanisms on metal surfaces.

## 1.3 Thesis Overview

This dissertation will focus on the unique properties associated with the self-assembly of various organic molecules on a Cu(111) surface. The investigations are mainly carried out with STM, which will be introduced in Chapter 2. The following Chapter 3 and Chapter 4 will discuss the influence of nanoscale confinements, provided by the cavities of anthraquinone networks, on CO molecules, with Chapter 3 focusing on the spatial distribution of CO inside the confinement, and Chapter 4 on the dynamics of confined CO. Chapter 5 will introduce a unique interlocking

pinwheel structure found for a propynenitrile molecule. Chapter 6 will include some recent results on metal-ligand coordination. Chapter 7 will discuss some related further studies that may be carried out in the future.

# 2 Experimental Method and Set-up

The experimental studies are carried out primarily on ultra-high vacuum (UHV) cryogenic scanning tunneling microscopy systems, with further confirmation from theoretical calculations. The basic principle of STM will be introduced in this chapter, as well as some STM specifics. Also sample preparations for experiments in this dissertation will be detailed.

## 2.1 Scanning Tunneling Microscopy

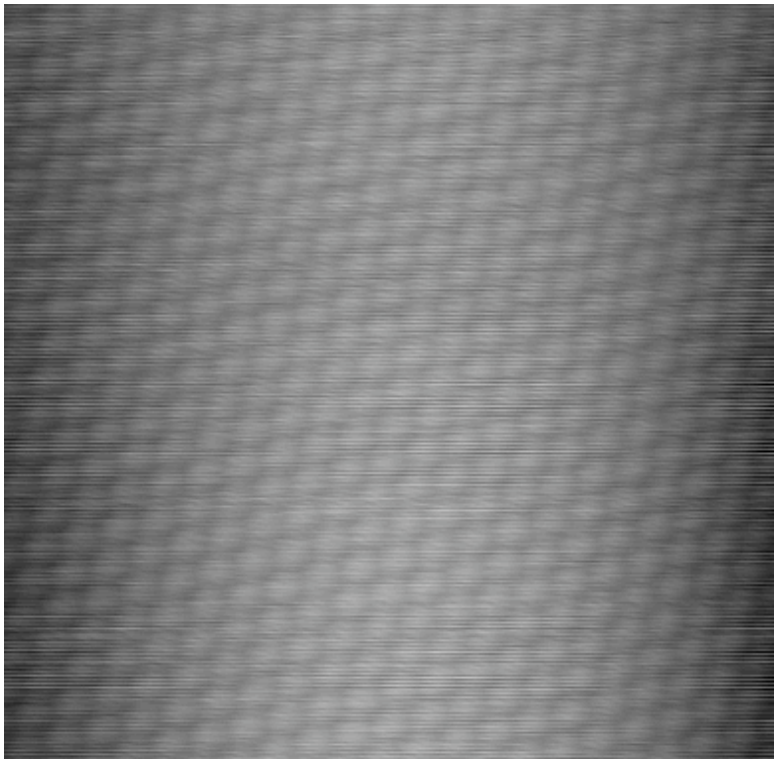

**Fig 2.1** Atomic resolution STM image of copper lattice on a Cu(111) surface. Image parameters, 7 nm × 7 nm; bias, −0.018 V; current, $6.1\times10^{-10}$A; temperature, 90 K .

STM is a very powerful tool for surface science studies. One of the most fascinating features is its sub-Ångstrom resolution that allows us to directly "see" individual atoms and molecules as well as the landscape of the surfaces (Fig. 2.1).[20,31] The following section will briefly discuss how it works.

### 2.1.1 Basic Principle

The atomic resolution arises from two aspects: 1) the extremely sensitive dependence of the tunneling current on the tip-sample distance originating from the tunneling nature of electrons, and 2) the exquisite control of the STM tip (and sample) displacement achieved by piezoelectric materials.

STM is based on the tunneling current between a sharp metallic tip and a conductive material. When the tip gets very close yet without physical contact to the sample surface, electrons have a finite probability to tunnel across the vacuum barrier. When a small bias voltage V (eV< $\phi_{sample}$ and $\phi_{tip}$ ) is applied and offsets the Fermi levels of the tip and sample, a net electron flow from the occupied states of the sample (or tip) to the unoccupied states of the tip (or sample) can occur, with the direction of the tunneling current determined by the polarity of the applied bias voltage (Fig. 2.2).[31]

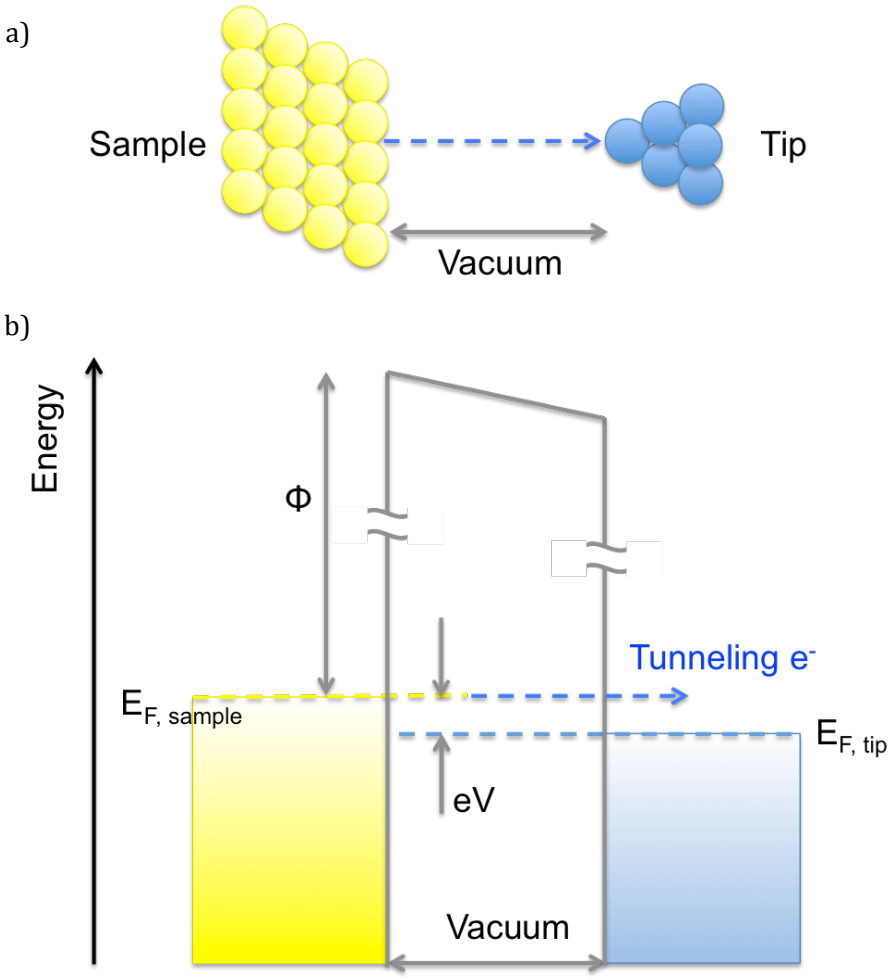


**Fig 2.2** Principle for electron tunneling in STM. (a) The tip and sample are separated by a vacuum barrier. (b) A bias voltage V offsets the Fermi levels of the sample and STM tip, allowing a net tunneling electron flow to occur.

In a crude approximation, the electron-tunneling phenomenon can be understood in one-dimension with a rectangular barrier, with the initial wavefunction

$$\psi_n(z) = \psi_n(0)e^{-kz},$$

where

$$k = \frac{\sqrt{2m_e(U-E)}}{\hbar},$$

with U the potential of the vacuum barrier, and E the energy of the electrons. The probability of electron tunneling from sample to tip (probability of observing the tunneled electron at z) can be expressed as

$$P = \left|\psi_n(z)\right|^2 = \left|\psi_n(0)\right|^2 e^{-2kz},$$

which gives the tunneling current

$$I \propto \sum_{E_n=E_{F-eV}}^{E_F} \left|\psi_n(z)\right|^2 \propto e^{-2kz},$$

(U-E) can be approximated as the sample work function $\phi$, when the bias voltage V is small, thus leads $k = \frac{\sqrt{2m_e\phi}}{\hbar}$. The work function $\phi$ is typically ~4-5eV for metals, which brings k to ~1Å$^{-1}$, suggesting that the current decreases one order of magnitude (or ~e$^2$) as the tip-sample distance increases by 1Å. [32,33]

The sensitive dependence of the tunneling current on the tip-sample distance is not the whole story of how the atomic resolution of the STM is achieved. In practice, to reach such a precise control of the displacement and motions of the tip and

sample, it is necessary to manipulate the sample and tip using piezoelectric materials.

Piezoelectric materials respond to an applied electrical voltage with a mechanical deformation. Quartz is a commonly used single crystalline piezoelectric material. Some polycrystalline ceramics also exhibit piezoelectricity, and can be produced through a polarization process in a strong electric field. [32] Lead zirconium titanate (PZT) ceramics are typically used in scanning probe microscopes, with a 10pm to 1Å resolution at a typical dimension.

In order to maintain a stable tunneling junction between the tip and sample, the system must be separated from any noise. STM systems are mounted on air tables that isolate them from ground vibrations. . This is important to obtain an undisturbed image.[32]

### 2.1.2 Functions

STM is very versatile and capable of various measurements and operations ranging from microscopy and spectroscopy to manipulation of molecules. Topographic imaging of the surface is one of the most commonly used features. Beyond that, it can take various spectroscopic measurements to investigate various properties such as molecular motion, electronic structure, or chemical identification.[20,31,34] The manipulation of individual atoms and molecules can also be realized with the STM.[35-40]

The STM typically measures the topography with a so-called "constant-current mode", which is to raster the tip across the sample surface while maintaining the current at a set point value, controlled by a feedback loop. Thanks to the sensitive dependence of the tunneling current to the tip-sample distance, the tip will faithfully follow the profile of the surface (Fig. 2.3). [31] A topographic map can be generated as the tip finishes scanning the area line by line.

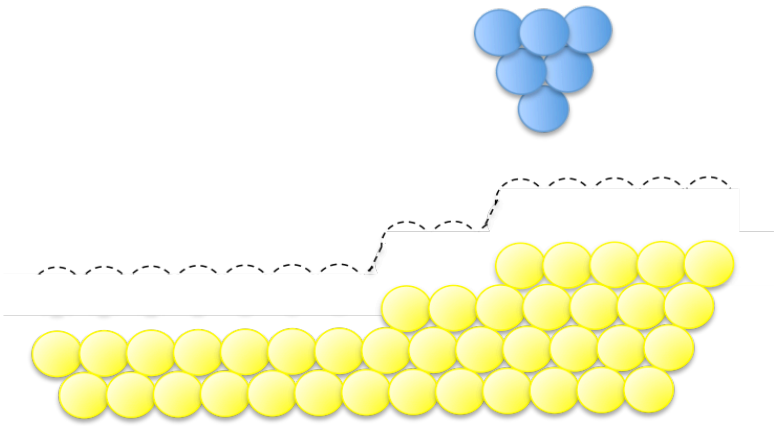

**Fig 2.3** A schematic model shows an STM tip working in the constant-current mode. To maintain a constant set-point current, the separation between the tip and sample is kept constant, making the tip faithfully follow the profile of the surface.

This provides a real space view of the surface and adsorbed molecules or atoms with sub-Ångstrom resolution, and thus offers a visual sense of the investigated system including the surface condition, molecular adsorption orientation, or supramolecular structures. Rotation and diffusion of molecules can also be investigated by repeated imaging of areas in which motion is happenning.[20-22,41-47] This is analogous to taking snapshots continuously of a moving scene, except it

typically takes about ~10s or longer for a STM to record each frame. Thus to study molecular motions without exceeding the STM data image speed limit, low-temperature conditions are generally applied to slow the molecular motions under study.[20]

Spectroscopic techniques are developed based on STM, mostly by placing the tip at a fixed position above a desired place on the sample (tip-sample distance within tunneling condition), and measure various relations such as tunneling current vs. time (I-t) relation, tunneling current vs. bias voltage (I-V) relation, dI/dV vs. bias voltage relation, or $d^2I/dV^2$ vs. bias voltage relation. From the obtained spectrum, information such as fast molecular motion, electronic structure and vibrational energy levels can be extracted. [7,20,31,48-54]

Manipulation of individual molecules and atoms is another fascinating feature of STM. Moving adsorbates on the surface is attempted through several different approaches; with strategies of increasing the tip-adsorbate interaction, injecting tunneling electrons, or applying electronic fields.[35-37,39,40,55-75] The lateral manipulation is essentially pushing or pulling the adsorbate with the STM tip. When the tip is brought very close to the adsorbate, the force in between can result in a lateral displacement of the molecule as the tip moves.[40,68,74] Vertical manipulation transfers the molecule to the STM tip and, applied reversely, drops it at a desired location, by applying an electric field to the adsorbate through the tip. The polarity, either induced or permanent, of the adsorbate can generate an electrostatic force to

grab and release it from the tip before and after the transport.[68] Tunneling electrons can induce desorption or selective bond breaking of individual molecules. Energy can be transferred to the molecule, with the injected electrons, through resonant states, and break the bond when the energy surpasses the bond's dissociation limit.[57,68]

## 2.2 STM Specifics

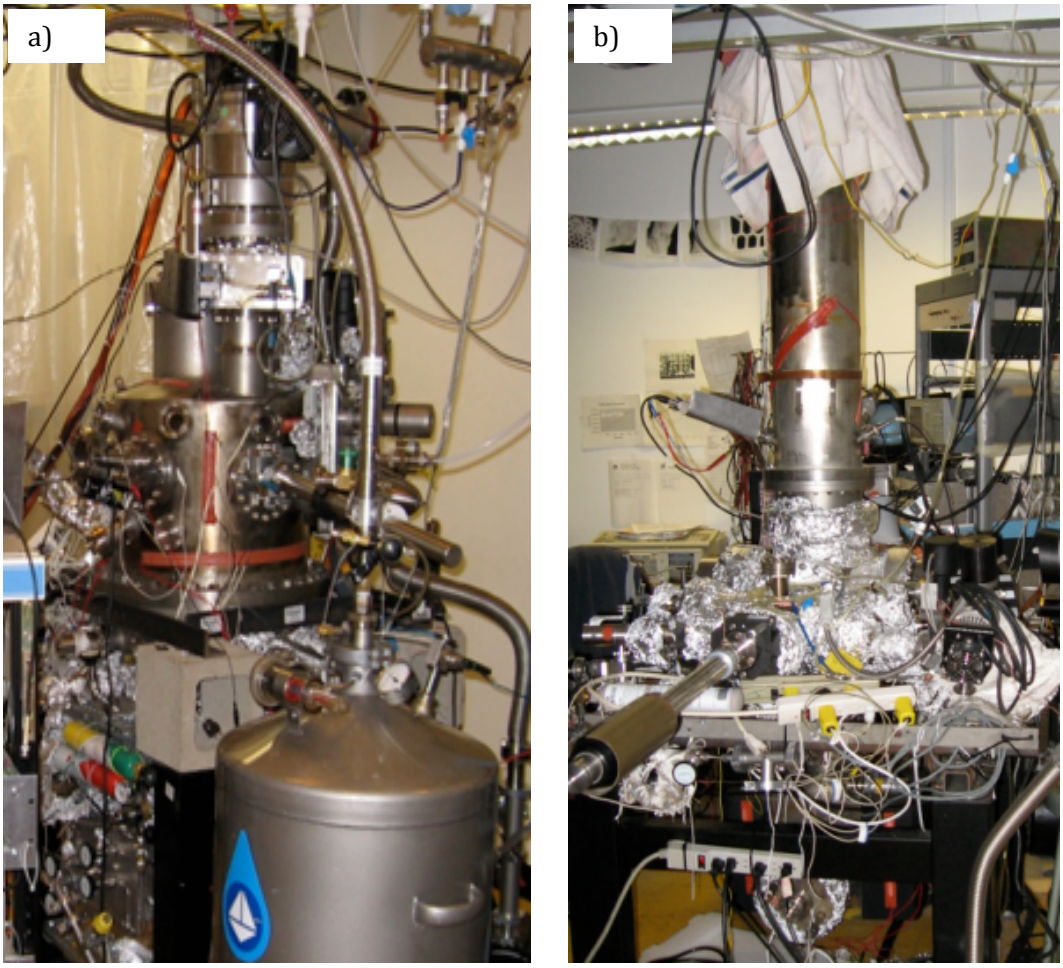


**Fig 2.4** Home-built ultra-high vacuum (UHV) STMs with two different cooling systems of (a) continuous flow and (b) bath cryostat, respectively.

There are two types of cryogenic STM systems in the Bartels lab, bath cryostat and continuous flow STMs. (Fig. 2.4) Both are in ultra-high vacuum (UHV) chambers, with a base pressure of $\sim 1\times10^{-10}$ torr. Each chamber is equipped with a 500L/s turbo pump as well as ion pump, sputter gun, ion gauge, mass spectrometer, and titanium sublimation pump (TSP).

It is very important to isolate the vibrations from the ground during STM measurement. To this purpose the tables of the whole systems can be floated with high-pressure gas (80psi in use). Turbo pumps are helpful during the sample preparation process, but will be stopped during STM measurement - i.e. only the ion pumps will be running when scanning - to avoid vibrations.

The major difference of the continuous flow and bath cryostat STM systems lies in the cooling system. The former can reach various temperatures ($\sim$10K to 298K) by varying the flow rate of the cryogenic liquid (i.e. He or $N_2$ liquid) cooling the dewars. While the latter keeps cryogenic liquid in dewars, thus provides only cryogenic liquid temperature (i.e. $\sim$80-90K for liquid nitrogen), or 298K when dewars are unfilled.

## 2.3 Sample Preparation

Preparation of the sample typically consists of two parts: substrate cleaning and molecule/atom deposition.

### 2.3.1 Cu(111) Substrate Preparation

UHV-STM measurements generally require clean and atomically flat surfaces. This can be achieved by cycles of sputtering and annealing the substrate in the UHV chamber. The smoothness and cleanliness will be checked by subsequent STM imaging.

The purpose of sputtering is to get rid of the unwanted adsorbates on the surface. Our typical sputtering procedure is first introducing Ar gas ($\sim 5\times10^{-5}$ torr) into the chamber after all pumps are either turned off or separated from the chamber by gate valves, then setting the emission and acceleration voltage on the ion bombardment gun controller at 20mA and 3kV, respectively. The Ar atoms will be ionized by the emitted electrons and accelerated by the high voltage to bombard the surface. Before each sputtering, a TSP is run for ~3 minutes to improve the vacuum.

The following thermal annealing is to make the bombarded surface smooth. After pumping out the Ar gas introduced in the sputtering step, the sample should be brought to a good vacuum condition (pressure at $\sim 1\times10^{-9}$ torr or lower). Then the sample is heated with a coiled tungsten filament at its back. The heating power is typically ~22 watts (15V×1.5A) provided by a DC power supply.

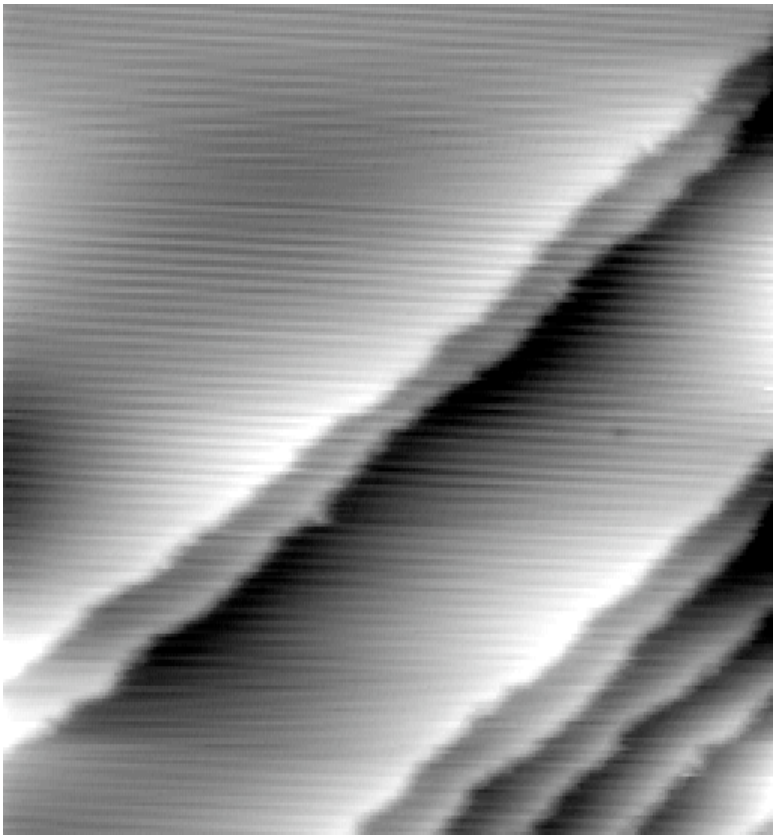

**Fig 2.5** STM image of a clean, atomically flat Cu(111) surface prepared with 8 cycles of sputtering & annealing treatment. Image parameters, 55 nm × 55 nm; bias, −0.8V; current, 78 pA; temperature, 90 K .

Both sputtering and annealing processes are maintained for 20 minutes and conducted in an alternating fashion for several cycles. The number of cycles depends on the sample conditions. Generally speaking, 6 to 10 cycles can make a clean and smooth sample for Cu(111). (Fig. 2.5)

### 2.3.2 Molecule Deposition

The deposition methods are slightly different for molecules with different vapor pressures.

Molecules with low vapor pressure ($<10^{-9}$ torr) at room temperature are typically in the solid phase. Heating is required to sublime the molecule to the metal substrate. The substrate is supposed to be aligned in a line-of-sight fashion with the molecule source in a glass capillary, to collect the beam of flying molecules more efficiently. It is noted that pretreatment of degasing is required to get rid of impurities with lower vapor pressures. This is generally conducted by preheating the molecule with a slightly higher temperature than that for sublimating to the substrate.

For molecules with higher vapor pressure ($>10^{-9}$ torr), heating is not necessary. Instead a leak valve is required to control the amount of molecules flying into the chamber. Freeze-pump-thaw cycles are needed to purify liquid samples, for the reason that quite a large amount of gas from the air could be dissolved in liquids. The procedures are- as indicated in the notation- first freezing the liquid (generally with a cooling bath of liquid nitrogen), followed by applying a vacuum condition, then thawing the molecules in a warm water bath to release the trapped bubbles of gas. 3 cycles is a typical minimum required. Additional cycles may be needed if there are still bubbles coming out from the solution during thawing.

# 3 Power of Confinement: Spatial Distribution of CO Molecules

This chapter is adapted from publication *Adsorbates in a Box: Titration of Substrate Electronic States.* Volume 105, Issue 6, 2010 Physical Review Letters.

Understanding the adsorption of molecular species at solid surfaces resonates as one of the unifying themes throughout the evolution of surface science over the past half-century. The adsorption of an ever-increasing number of molecules on crystallographic surfaces as well as on steps and at other defect sites, has been studied. Great progress has been made in the development of computational techniques that reveal the electronic interaction between adsorbates and the underlying substrate atoms. However, the effect of lateral confinement of the support on the nanometer scale has remained largely unaddressed because of challenges in the preparation of surfaces covered with atomically identical patterns several nanometers in scale and because of computational limitations in simulating systems consisting of many hundreds of substrate and adsorbate atoms. Yet many of the applications of surface science, for instance in heterogeneous catalysis or in semiconductor processing, crucially rely on nanoscale-delimited surfaces; and recent progress in these fields emphasizing the effects of nanoscale confinement[76] and diminishing scale, respectively.

In this chapter how confinement of the substrate to approximately 4 nm hexagons affects the distribution and energetics of small molecule adsorption will be addressed. The confinement is larger than most adsorbate patterns[7,12] and substrate unit cells but smaller than previously investigated structures such as quantum corrals and adislands,[77,78] affects the distribution and energetics of small molecule adsorption.

It has been shown that perturbation of substrate electronic states, such as an underlying gas bubble[79] or scattering of a Shockley surface state at a step edge[80]or adatom row[81], affect adsorbate distribution. Substrate-mediated long-range interactions between molecules have been found in a variety of systems and quantified in a number of cases.[15,82-91] A correlation between the location of CO molecules on Ag(111)[92] and benzene on Cu(111)[80] with the phases of the surface scattering amplitude have been proposed from experimental data and through theoretical modeling.[93,94] This experimental study shows that confined electronic states of the substrate can actually be titrated with adsorbates, arguably much as electronic states are filled up from the lowest to highest energy in an atomic orbital diagram.

## 3.1 Nano-scale Pores

The measurements were conducted on a Cu(111) surface decorated with an anthraquinone network. The 9,10-anthraquinone molecules are found to self-assemble into a chiral network of six-fold symmetric (disregarding the substrate) on

the atomically flat Cu(111) surface (Fig. 3.1). The network exhibits hexagonal pores with the diameter as large as ~4nm that expose 186 substrate atoms in their midst. Also it is found robust enough to sustain coadsorption of small molecules, such as CO and $H_2O$.[15]

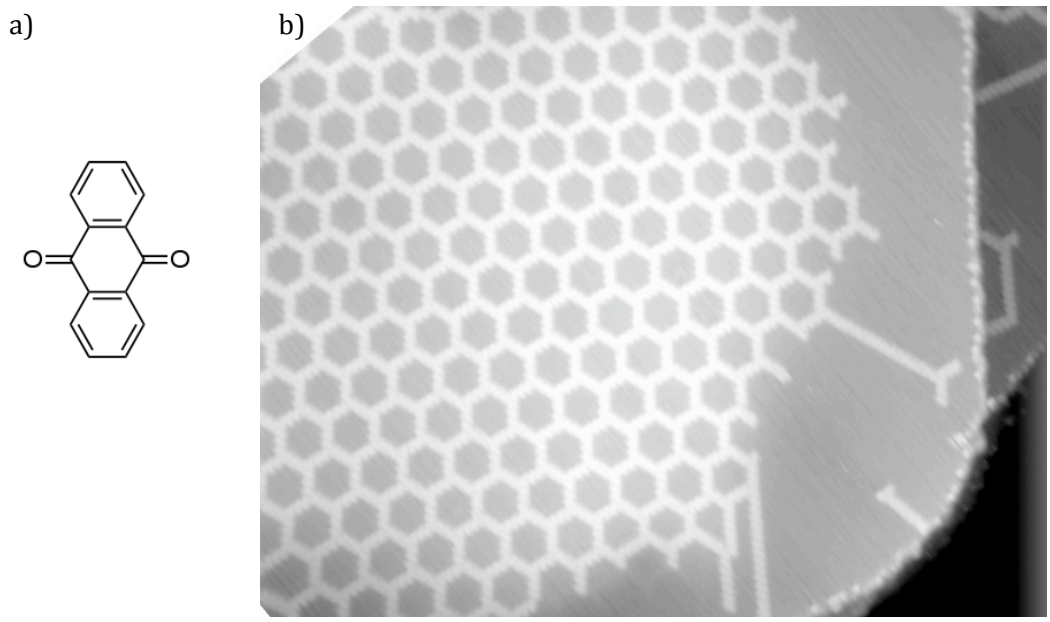


**Fig. 3.1** (a) Chemical structure of the 9,10-anthraquinone molecule; (b) Self-assembled anthraquinone network on Cu(111) surface. Image parameters, 83 nm × 73 nm; bias, −2.53 V; current, 50 pA; temperature, 90 K .

CO is used as the test molecule because a wealth of data on its surface behavior is available: CO molecules adsorb upright atop Cu(111) substrate atoms. They are imaged in scanning tunneling microscopy (STM) as protrusions or indentations, depending on whether the STM tip is decorated with a CO atom at its apex or not, respectively.[95]

Sample preparation involves the usual sequence of sputtering and annealing, followed by cooling to liquid nitrogen temperatures. The anthraquinone pattern is created by evaporation of the molecule onto the cryogenic sample followed by annealing to room temperature. Deposition of CO molecules through a leak valve onto the anthraquinone-patterned surface at 40K preserves the pore shapes.

### 3.2 Spatial Distribution of CO in Pores

The anthraquinone network is found to block the diffusion of adsorbed CO molecules on the substrate; repeated imaging of the same set of pores allows tracking of the perambulation of a fixed number of molecular entities within a confined area. Fig. 3.2 shows snapshot images from a movie on a set of pores, in each of which a few molecules are seen to diffuse.

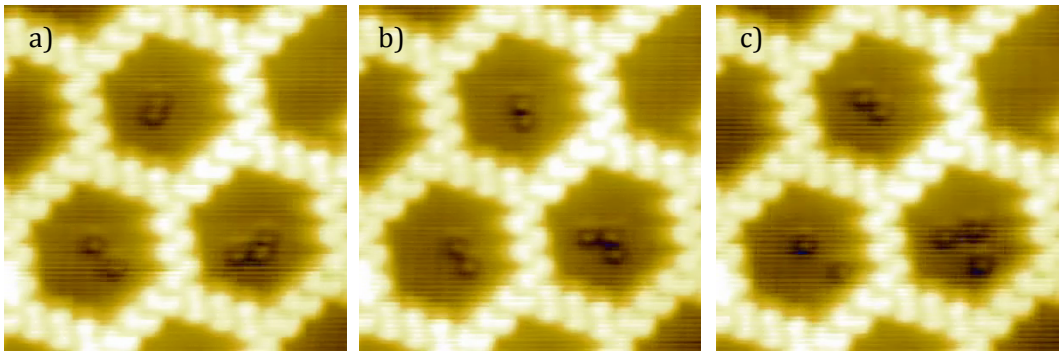


**Fig 3.2** (a,b,c) Snapshot images from a STM movie showing the diffusion of two and three CO molecules in confinement. Image parameters: 6 nm x 10 nm; Bias: -2.673 V; Current: 99 pA.

In such sequences of images each molecule can be assigned to a particular substrate atom on which it is adsorbed. From thousands of images obtained, histograms of the occupation of the various substrate sites within the confined area are calculated (Fig. 3.3a-e). Each confined area consists of 62 threefold degenerate (186 in total) adsites surrounding a hollow site at the pore center in a threefold symmetric arrangement. The anthraquinone network is chiral, preventing inversion symmetry.

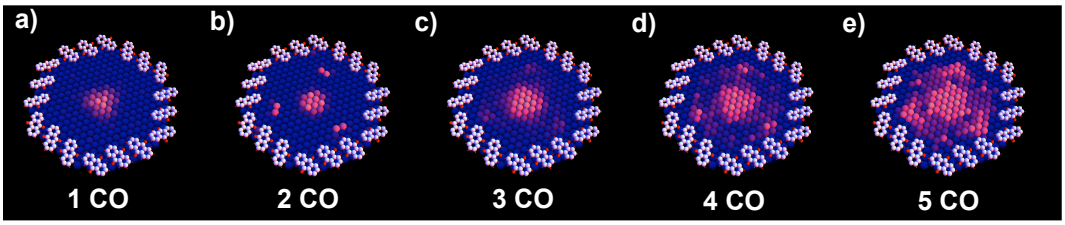


**Fig. 3.3** Color-coded plots of the probability of CO molecule occupation for each of the 186 Cu substrate atoms exposed within an anthraquinone pore. Each plot is based on > 500 CO configurations observed and averaged over equivalent locations.

The radial distribution of CO molecules in pores of different coverages is shown in Fig. 3.4. Given the large number of different adsites, 7 radial bins, as constructed by J. Wyrick, are indicated in the inset of Fig. 3.4. In pores containing a single CO molecule, the CO is generally found at the pore center; in 54% of the cases, the molecule occupies one of the two inner bins of Fig. 3.4.

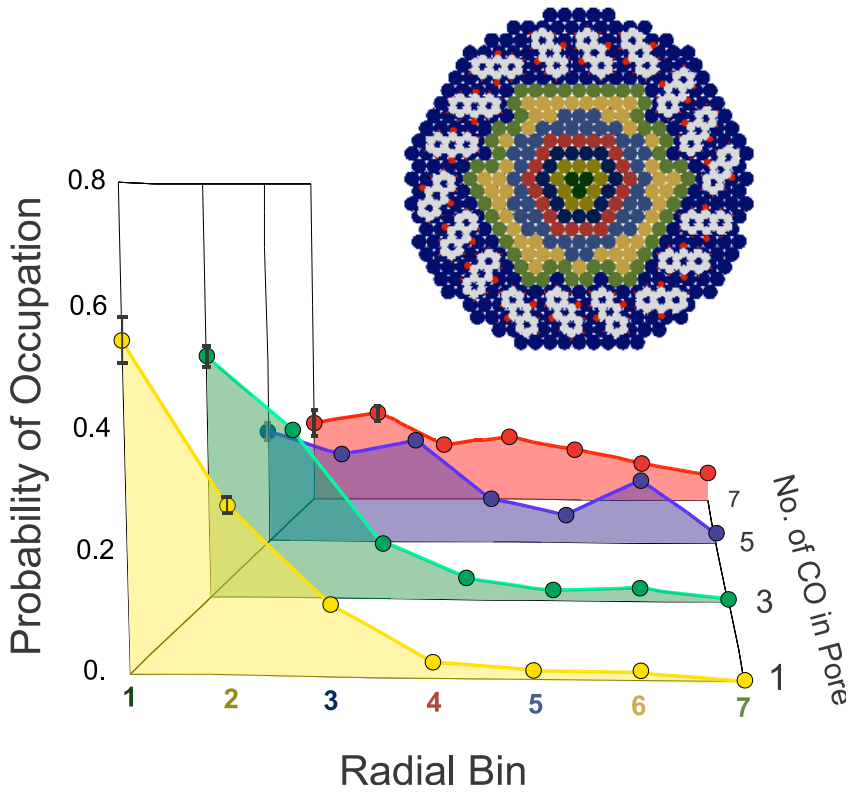


**Fig. 3.4** Normalized probability of occupation of radial bins (shown in the inset) for pores containing 1-7 molecules. For 1,3 molecules the distribution is monotonic, whereas at increasing number of molecules also an additional intermediate distance becomes favored until further increase of the coverage renders the plot featureless. Error bars are based on √counts in the histogram and are shown when larger than the data markers.

From the distribution of Fig. 3.3a, the radial variation of the probability $P_i$ of CO occupation of an adsite i (indicated in the yellow (front) curve of Fig. 3.4) is obtained. From this dataset the canonical partition function Z of the single CO system can be

constructed, which allows the deduction of the radial variation of the CO adsorption energy ε (Fig. 3.5).

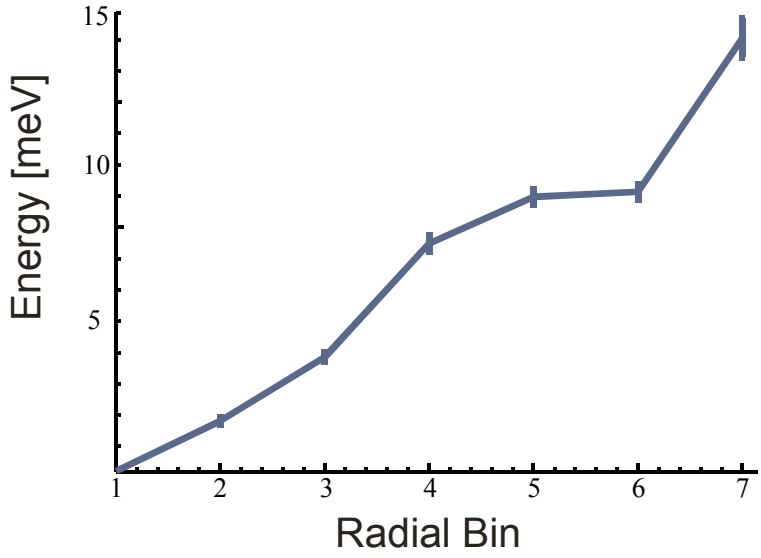


**Fig. 3.5** Variation of the adsorption energy of a single CO molecule across a pore. Error bars are based on √counts in the histogram and are shown when larger than the data markers.

$$Z = \sum_i e^{-\varepsilon_i / kT} \quad with \quad P_i = e^{-\varepsilon_i / kT} / Z$$

with k the Boltzmann constant and T the temperature 27 K of the measurements. The resultant variation of ≈ 14 meV is quite substantial, approximately 1/5 of the CO/Cu(111) diffusion barrier of 75 meV.[85]

For two CO molecules in the system (Fig. 3.3b), it is generally found that either both molecules occupy the confinement center or they are split between the center

sites and a set of three equivalent adsites approximately halfway towards one set of confinement vertices. The same set of three adsites is also favored in pores that contain 3-5 molecules (Fig. 3.3c-e). Experimentally, these are independent datasets acquired on different pores, days and sample preparations; the reappearance of the same location for pores of different coverage rules out experimental error (e.g. through subsurface defects) as the origin of the peripheral peaks in Fig. 3.3. This poses the question of their physical origin and, in particular the reason for their threefold symmetry. The ≈ 4nm diameter of the pore rules out direct intermolecular interactions, suggesting that a substrate-mediated effect may be of relevance. Unfortunately, first-principles computational methods (such as density functional theory) are incapable of treating a system that requires at least 186 substrate atoms per layer (i.e. several hundred in total). Thus, a continuum model of the substrate electronic setup focusing on the Cu(111) surface state is resorted to. In this context it is important to realize that although the pore boundary itself is sixfold symmetric, the pore vertices are alternatingly centered on hcp and fcc hollow sites, so that the overall symmetry of the pore on the substrate has the same threefold (and not sixfold) symmetry of the CO distribution.

The calculation of confined electronic states within the pore, as carried out by J. Wyrick and collaboration with T.L. Einstein's group at University of Maryland, starts from the known solutions of a particle in a triangular box[96], followed by relaxation into the actual geometry of the pore. Gross et al. showed that scattering of the

surface state from organic molecules occurs not at the peripheral hydrogen atoms but at the 2nd period elements.[97] Hence, the boundary of the pore from the six carbon and oxygen atoms per molecule (102 in total) that are closest to the pore center is constructed. An iterative finite-difference algorithm[98], more commonly used for solution of Poisson or heat-diffusion equations, to the relaxation of the known solutions into the geometry of the pore is adapted. Here, the wave function in a Taylor series to third order is developed; summing over four locations adjacent to a point (x,y) reproduces the Hamiltonian $H_{inside}$ inside the potential- free pore.

$$\frac{\langle x+\delta, y| + \langle x-\delta, y| + \langle x, y+\delta| + \langle x, y-\delta|}{\delta^2}|\varphi\rangle - \frac{4\langle x, y|\varphi\rangle}{\delta^2} \cong \frac{-2m^*}{\hbar^2} H_{inside}|\varphi\rangle = \frac{-2m^*}{\hbar^2} E|\varphi\rangle$$

with m* the effective mass of an electron of the surface state of 0.34 electron masses and d a small displacement. Thus, if $\varphi_{n-1}$ is an approximate eigenfunction of the Hamiltonian, a better approximation $\varphi_n$ can be found by evaluating

$$\langle x, y|\varphi_n\rangle = \frac{\langle x+\delta, y| + \langle x-\delta, y| + \langle x, y+\delta| + \langle x, y-\delta|}{4 - 2m^*\delta^2 E_{n-1}/\hbar^2}|\varphi_{n-1}\rangle$$

Alternating this iteration and Gram-Schmidt orthogonalization[99] of the set of eigenfunctions originally obtained from the triangular particle in the box problem, it ends up with three eigenfunctions (one unique and one twofold degenerate) whose eigenvalues E of 170 meV and 440 meV, respectively, are below the Fermi Energy $E_F$, if measured from the bottom of the surface state band of 450 meV below $E_F$.[100,101] Fig. 3.6a,b shows the distribution density of state associated with the first and

twofold-degenerate second state, respectively. The algorithm provides correct eigenfunctions and – states that are converged and invariant to the grid spacing d of 1.25 Å, 0.63 Å, or 0.41 Å (corresponding to using a 40x40, 80x80 or 120x120 points grid to represent the pore); however, it cannot guarantee completeness of the set of eigenfunctions/-values found. Summation of the fraction of the surface Brillouin zone filled by the surface state (characterized by the Fermi vector $k_F$ = 0.21 Å$^{-1}$)[101,102] over the exposed substrate atoms leads to no more than 3 complete electron pairs in the surface state within each pore, in good agreement with the three states found. This result is further corroborated by the finding of Lobo-Checa et al. by electron spectroscopy that there is exactly one confined state in a molecular surface network of roughly 1/3 the size of the system described here.[7]

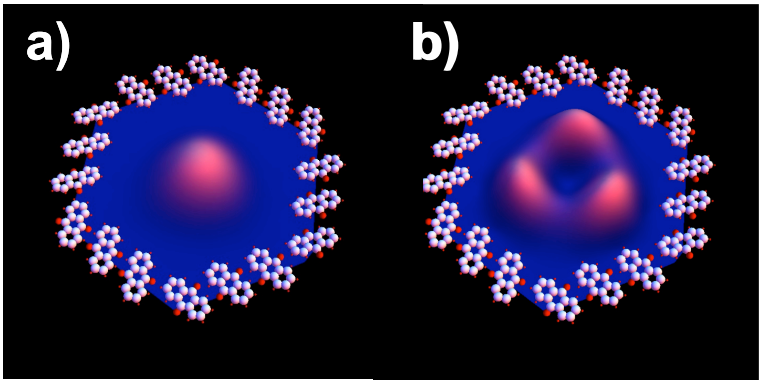


**Fig. 3.6** (a,b) Plot of the local density of states of the first and twofold-degenerate second electronic state of the pore, respectively. Compare to the distribution of molecules in pores in Fig. 3.3.

Comparison between the density of state of Fig. 3.6 and the molecular distribution within the pore of Fig. 3.3 reveals a remarkable correspondence. Moreover, the sequence of lateral arrangements of CO molecules found when 'titrating' the pore with an increased number of molecules, i.e. first filling the pore center and subsequently the peripheral states, matches the energetic order of the surface state density of states so that the filling of CO molecules into the pore is reminiscent of filling electrons into an atomic orbital diagram. While previous work on the interaction of adsorbates with the surface state focused on comparison with the lateral surface state distribution at $E_F$ visible in STM, the energy integrated approach afforded by the small scale of the pore provides a much more complete understanding of the underlying physics.

Increasing the number of molecules inside the pore beyond the number of electrons in the surface state (i.e. 6) causes the radial distribution of molecules in the pore to become more uniform (red curve in Fig. 3.4), showing the limitation in adsorbate guidance achievable in a pore of given size. This finding corresponds with CO's ability of quenching the surface state at relatively low coverage.

Although the calculations were based on free-electron-like behavior of the surface state electrons (i.e. a constant potential within the pore boundary) with just an effective mass accounting for the presence of the substrate, the finding of threefold symmetry (as enforced by the substrate, in contrast to the sixfold symmetry of the molecular network) is crucial for explaining the experimental

distribution of adsorbates; this highlights the limitation of the free electron approximation in understanding surface state electrons and their impact on adsorption.

By monitoring adsorbate diffusion within a nanometer-scale confined system, it is found that such confinement has a pronounced effect on their average location, suggesting that engineering of confinement boundaries may not only allow engineering of surface electronic states but can also be a tool in assembling molecular patterns at surfaces.

# 4 Power of Confinement: Dynamics of CO Molecules

This chapter is adapted from publication *Power of Confinement: Adsorbate Dynamics on Nanometer-Scale Exposed Facets.* Volume 10, Issue 9, 2010 Nano Letters.

The diffusive behavior of adsorbates has generally been studied on extended terraces, that is, not under lateral confinement, mainly due to experimental impediments, yet metal clusters with nanoscopic facets have considerable technological relevance, for instance as supported metal catalysts for applications ranging from the (petro-)chemical industry to emission control. For the study of the dynamics of adsorbates on nanoscale clusters, it would be ideal if arrays of atomically identical ones could be formed. Absent this possibility, a Cu(111) substrate covered with a self-assembled anthraquinone network is utilized.

The pores have a similar size as the facets expected on catalytic nanoclusters; in particular, studies on gold have shown that its activity increases enormously if dispersed in this size regime.[103,104] Conventionally, the high activity of nanoparticles, as compared to the surfaces of bulk metals, is attributed partly to the high surface to volume ratio at high dispersion, and partly to support-metal interactions and to the abundance of surface defect sites such as step-/facet-edges and -kinks.[105] While the exposed copper facets of the anthraquinone network probably have little besides their size in common with catalytic nanoparticles, they nevertheless open for study the kind of effects that lateral confinement may have on the dynamics of adsorbates,

at least in a phenomenological manner; a survey of them is the objective of this study.

Several previous publications addressed the dynamics of adsorbates at metal surfaces and their interaction with one another. They include measurements of the dynamics of benzene molecules,[106,107] reactive mixtures,[108,109] hydrogen atoms,[110] and CO molecules.[85,86,92,111-113] Also, the insertion of atoms or molecules into molecular surface networks has been studied previously.[5,12,114-117] What makes this study novel is the confined nature of the adsorbates that allows studies on how molecules behave when their support is not a large, clean, and inert terrace.[118]

CO is used as the test molecule because abundant data on its surface behavior is available, as mentioned in Chapter 3 and literature.[95] At sufficient coverage, CO adsorbates form an ordered $(\sqrt{3} \times \sqrt{3})R30°$ overlayer; large islands of this superstructure have been observed in previous STM studies.[119] In the model system there are 186 exposed atop adsites in each 4 nm pore, allowing a maximum occupation in the exposed facet of 62 CO molecules in a dense $(\sqrt{3} \times \sqrt{3})R30°$ adlayer.

Initial sample preparation involves the usual sequence of sputtering and annealing, followed by cooling to liquid nitrogen temperatures. The anthraquinone pattern is created by deposition of the molecule onto the cryogenic sample followed

by annealing to room temperature. After subsequent cooling to ~40 K, CO is deposited through a leak valve.

## 4.1 Diffusion of CO at Full Coverage

Deposition of CO molecules into an anthraquinone honeycomb network does not alter the pore shape. With careful dosage, a CO coverage very close to a complete $(\sqrt{3} \times \sqrt{3})R30°$ overlayer is obtained, which is visible inside the pores (Fig. 4.1). Moreover, a dislocation line is found on the exposed facets, which is constantly present yet persistently shifting position. This differs from the behavior of CO films on extended terraces, where the $(\sqrt{3} \times \sqrt{3})R30°$ is observed over large areas and dislocation lines (i.e., antiphase domain boundaries) are expelled to the edge.[119] What is the origin of this effect?

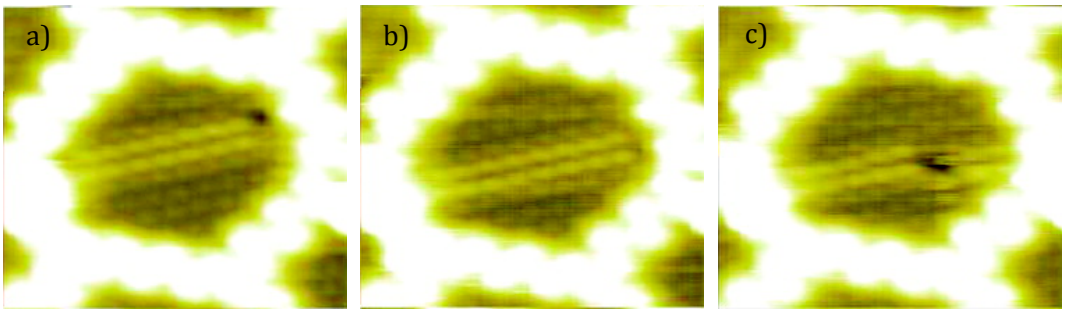


**Fig. 4.1** Images from a STM movie of a constantly existing dislocation line moving in confinement. Image parameters: bias −2.40 V; current 44 pA; temperature, 24 K.

Each exposed facet is centered around a substrate hollow site, allowing three equivalent atop adsites (light blue in Fig. 4.2a to anchor the CO $(\sqrt{3} \times \sqrt{3})R30°$ pattern, thus spanning three equivalent overlayer sublattices. The facet edges consist of two alternating sets of three equivalent sides, much as any hexagonal fcc island is surrounded by steps with alternating (111) and (100) facets. One of the sets of sides is equally decorated with CO molecules no matter which central substrate atom anchors the overlayer. Of the other set of sides, however, only two are covered intimately, leaving open space near the third side (yellow in Fig. 4.2a).

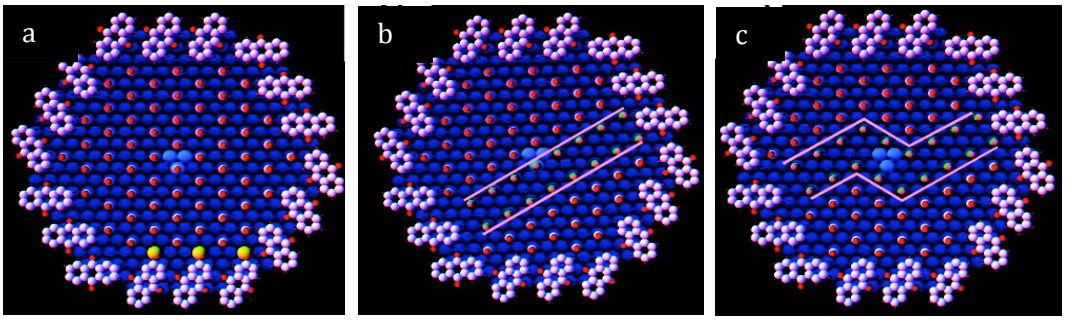


**Fig. 4.2** The $(\sqrt{3} \times \sqrt{3})R30°$ adlayer can be anchored at any one of the three atoms at the center of the exposed facet (light blue). In each case, one facet edge is decorated differently than the remaining two of the same kind (yellow in a). This can be alleviated, if a dislocation line is induced in the pore (b). In both cases, the same number of molecules fit inside the pore. (c) Model of a kink in a dislocation line similar to the STM image of Fig. 4.1 c.

The open space can be avoided if the CO adlayer is imperfect; a dislocation line in the overlayer allows placement of adsorbates at all sides of the second set

equivalently. Consequently, the confined adlayer is under competition between forming the structure found on extended surfaces and incorporation of a dislocation line that permits equal filling of the edge sites, that is, providing optimal edge interaction at the expense of intermolecular interaction. In both cases, the same number of CO molecules fit onto the exposed facet. The observation of the persistence of the dislocation lines indicates that the interactions at the adlayer edge are dominant over those within the adlayer.

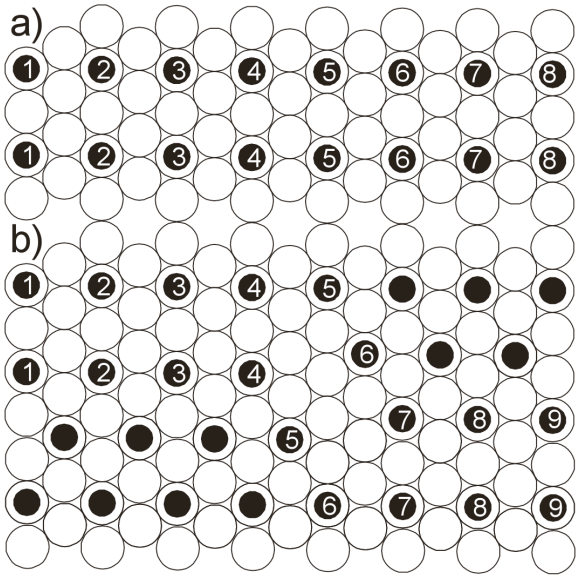


**Fig. 4.3** A dislocation line in a $\sqrt{3}x\sqrt{3}R30°$ overlayer without (a) and with (b) a kink. Introduction of a kink leads to two additional molecules affected by the dislocation line.

Imaging 75 setups of one dislocation line at 24 K, a kink is found to present in the line in ≈40% of the cases. A dislocation typically affects 16 molecules (8 per side, Fig. 4.3a); a kink in the double line increases this number by 2 along the dislocation

line (Fig. 4.3b). Analyzing the measured fraction of kinked lines using the Boltzmann equation and taking into account the degeneracy of the various possible kinked configurations, a kink energy of 6.1 ± 0.3 meV and a total energetic cost of the entire dislocation line of ≈0.05 eV is estimated. For three molecules, the edge-interaction is improved by the dislocation line (yellow in Fig. 4.2a). This yields a lower boundary of the edge interaction of ≈0.02 eV per molecule, a considerable energy compared to, for example, the CO diffusion barrier of 0.075 eV.[85]

The presence of the dislocation can potentially affect the chemical reactivity of the film markedly; molecules affected by a dislocation line have a nearest neighbor configuration that allows more ready access to them as well as the underlying substrate. The number of molecules affected by the dislocation scales linearly with the size of the facet, whereas the total number of molecules scales quadratically, indicating that the smaller the facet size, the more pronounced this effect. For the 4 nm facets studied here, the dislocation line is directly affecting more than one-fourth of the adsorbates (16 out of 62), significantly greater than on extended terraces.

## 4.2 Diffusion of CO at Lower Coverage

The constant motion of the dislocation lines well below 30 K contrasts substantially with the behavior of individual CO molecules on Cu(111), whose diffusion starts only at ≈33 K.[85] Is this effect limited to dislocation lines? For prepared films of slightly lower coverage with facets that have a small number of

vacancies in their ($\sqrt{3} \times \sqrt{3}$)R30° coverage (Fig. 4.4a-c), rapid motion at similarly low temperature is observed.

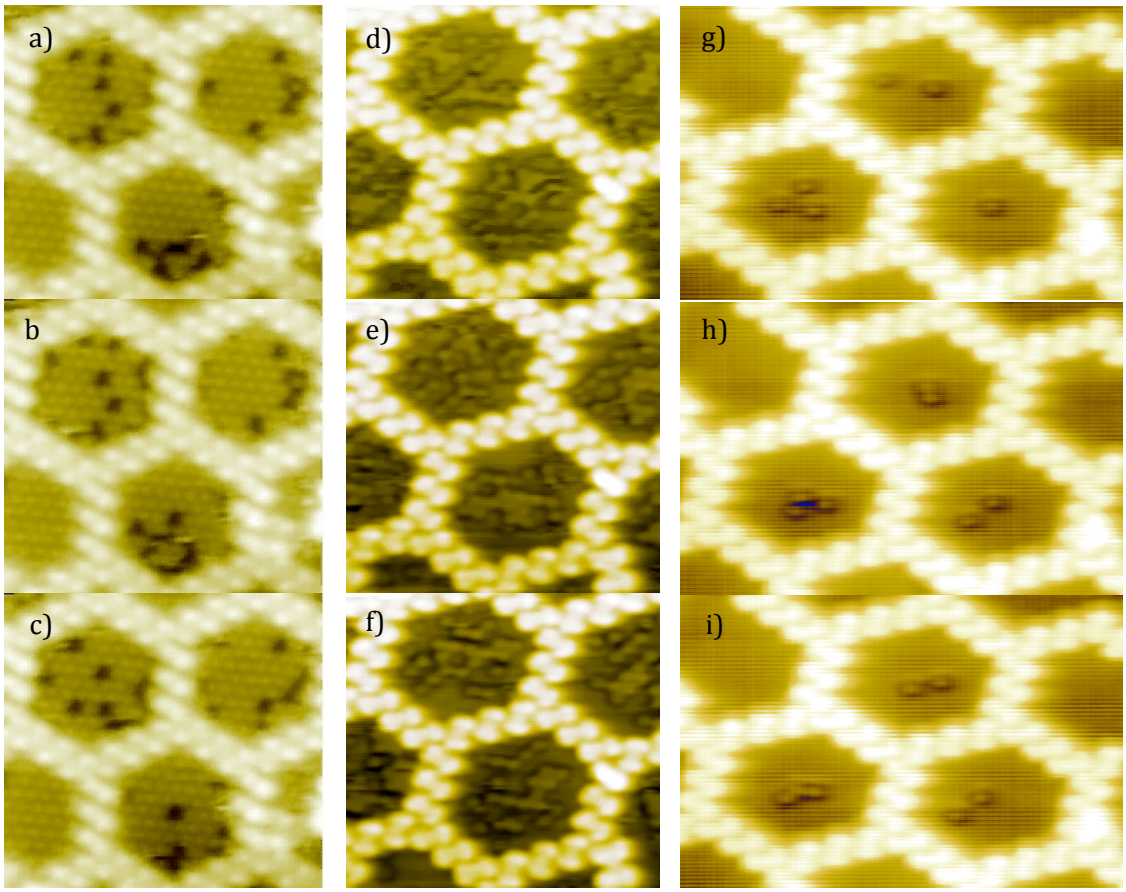


**Fig. 4.4** Images from STM movies showing the diffusion of (a,b,c) vacancies in a ($\sqrt{3} \times \sqrt{3}$)R30 °CO coverage in confinement (image parameters, 12 nm × 9 nm; bias, −1.23 V; current, 120 pA, temperature, 23 K). (d,e,f) Twenty to twenty-two CO molecules on each exposed facet (image parameters, 8 nm × 8 nm; bias, −0.72 V; current, 60 pA, temperature, 22 K). (g,h,i) Two and three CO molecules in confinement (image parameters, 12 nm × 9 nm; bias, −2.67 V; current, 100 pA, temperature, 27 K).

While increased diffusivity at high coverage has been observed in the past, it has not yet been quantified except at very low concentration[85] and for direct neighbors.[87,112 120] The confined nature of the exposed facets allows monitoring the diffusion rate for a fixed number-density of molecules.

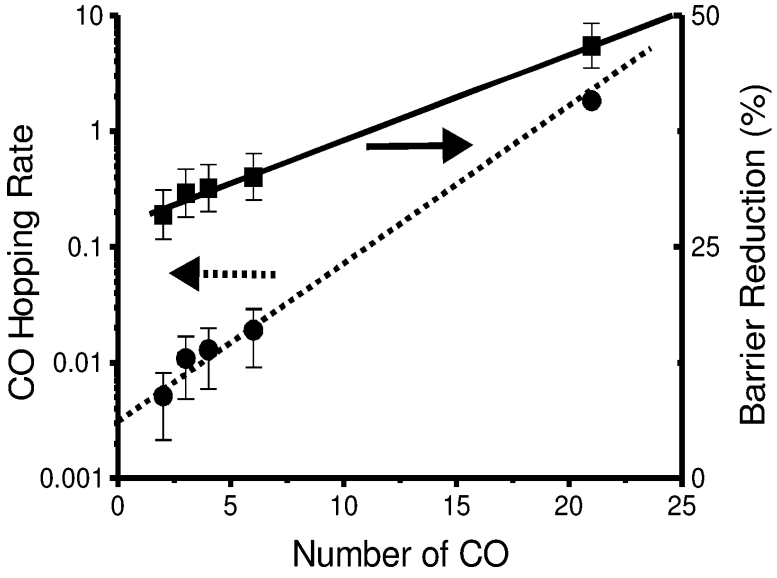


**Fig. 4.5** Dotted line: diffusion rate per molecule as a function of number of molecules on an exposed facet. Solid line: reduction of the diffusion barrier that causes this acceleration under the assumption of a constant diffusion prefactor. All error bars are dominated by the temperature uncertainty of 1 K in the measurements; the statistical error is much smaller than the data markers.

The dotted line of Fig. 4.5 shows the diffusivity from a few molecules per pore (Fig. 4.4g-i) up to the point at which the $(\sqrt{3} \times \sqrt{3})R30°$ adlayer is one-third complete and site blocking becomes important (Fig. 4.4d-f). While data points for

coverages up to 6 molecules on the exposed facet were measured at 27 K, diffusion at higher coverages was too rapid at this temperature; the data point for 21 molecules per pore was measured at 22 K and scaled according to the Arrhenius parameters of ref [85]. The dotted line represents an exponential fit of the diffusivity.

### 4.3 Discussion

A detailed look at the STM images indicates that the diffusivity depends not only on the number of molecules on the exposed facet but also on the position of the molecules within that facet. Generally, molecules tend to move less if they are closer to the center and more rapidly around the perimeter. Unfortunately, this renders a complete Arrhenius-based evaluation (which would need to separate molecules by location) beyond reasonable effort.

Thermally programmed desorption experiments showed that an increase of the surface coverage can lead to a reduction of the adsorption energy.[105] In the simplest approximation, the diffusion barrier is a constant fraction of the adsorption energy. While this argument justifies a variation of the diffusion barrier with coverage, it provides little indication that the diffusion preexponential factor should vary markedly with it. Fixing the diffusion prefactor at the value for isolated molecules,[85] the variation of the diffusion barrier with coverage can be obtained from the diffusion data (Fig. 4.5, solid line). The adsorption and subdivision of the Cu(111) terrace by the anthraquinone network causes a reduction of the CO diffusion barrier

by one-fourth; increasing the coverage inside the pore up to one-third of the ($\sqrt{3} \times \sqrt{3}$)R30° adlayer reduces the diffusion barrier by another one-fourth. The data suggests a linear fit of the reduction of the barrier as a function of the coverage with a slope of (57 ± 14)%/ML, with 1 ML defined as the complete ($\sqrt{3} \times \sqrt{3}$)R30° coverage. If the adsorption energy is assumed to be proportional to the diffusion barrier, then its reduction by half indicates a comparable reduction of the adsorption energy. The observation of a linear dependence of the energy reduction on the number density of molecules suggests that its origin is not direct pair interactions (which scale quadratically with coverage) but involves the substrate, potentially both through confinement-induced surface state effects[7,77,100] or through mediation of trio and higher order interactions.[93] While the effects of site blocking and nearest neighbor interactions prevent obtaining experimental data beyond 1/3 ML coverage, the results suggest a quite substantial destabilization of the CO molecules in the ($\sqrt{3} \times \sqrt{3}$)R30° adlayer, well in line with the results discussed in refs [105,120]

Following this discussion of the CO dynamics, the locations that the molecules/vacancies occupy and the effect of the lateral confinement on them are finally examined. To this end, the distribution of vacancies in coverages like the one shown in Fig. 4.4a-c and of molecules in coverages like shown in Fig. 4.4d-f is studied.

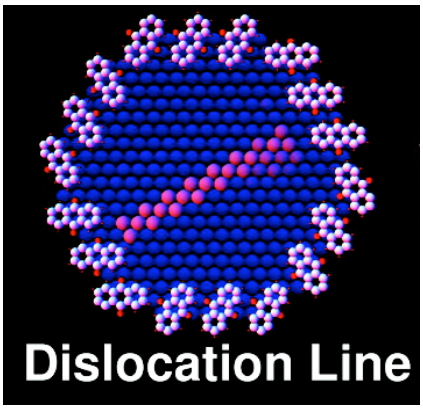


**Fig. 4.6** Dislocation lines (colored in pink) are most commonly found to cross the facet center of the anthraquinone pore.

Fig. 4.6 shows the likelihood that the dislocation line of Fig. 4.1 occupies different substrate sites in a color-coded histogram. In this context, it is important to realize that although the anthraquinone network appears 6-fold symmetric, due to the 3-fold (and not 6-fold) symmetry of the substrate, every other of its sides comes to rest at different surface locations. The dislocation line generally crosses near the center of the exposed facet thereby connecting dissimilar edges. Consequently, the area showing higher occupation of the dislocation line in the center right of Fig. 4.6 is not equivalent to the area on the center left of the pore line. The sensitivity of the dislocation line to the geometry of the facet boundary is a testament to the importance of confinement for the spatial distribution of adsorbates.

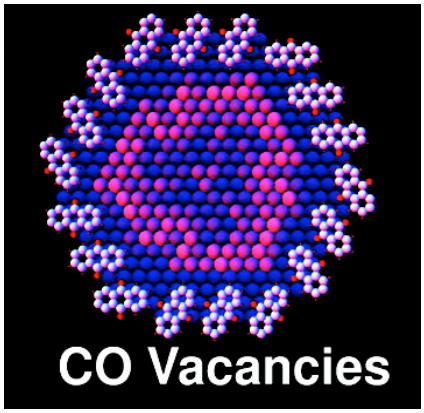


**Fig. 4.7** Color-coded histogram of CO vacancy (colored in blue) distribution for each of the 186 Cu substrate atoms exposed within an anthraquinone pore. The anthraquinone pore is chiral and 3-fold symmetric, the histogram are averaged over three equivalent rotational orientations. Vacancies are more commonly found around the facet edge.

Fig. 4.7 shows the distribution of vacancies on exposed facets a few molecules short of saturation; bright colors correspond to a high likelihood of finding vacancies. Viewing a large number of movies with coverages similar to Fig. 4.4a-c, the vacancies frequently arrange themselves in rows that originate at the facet edge and often bend back toward the same or an adjacent edge is qualitatively observed. In the histogram of Fig. 4.7, this is reflected in a higher probability for vacancies to be found at the edges with a slight preference for one kind of edge and vertex. It is important to realize that the vacancies do not segregate from the adlayer, that is, they do not form a closely covered area surrounded by empty space as on extended terraces. [119] Rather the vacancies are interspersed with the adlayer, affecting a far

greater fraction of the adlayer molecules and potentially rendering the adlayer more reactive. A statistical analysis of vacancy motion is much more complicated than for adsorbate motion, as in the $(\sqrt{3} \times \sqrt{3})R30°$ overlayer "fractional" vacancies (corresponding to molecules adsorbed in antiphase) can combine and molecules can occasionally and intermittently adsorb closer than the $\sqrt{3}$ spacing, so that the total number of vacancies on an exposed facet is not conserved.

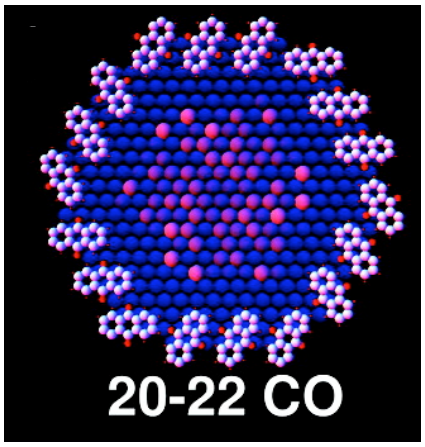


**Fig. 4.8** Color-coded histogram of CO molecule (colored in pink) distribution within an anthraquinone pore. For 20–22 CO molecules, a relatively featureless distribution is observed.

Reducing the coverage to 20–22 molecules on the exposed facet (i.e., ≃1/3 of the $(\sqrt{3} \times \sqrt{3})R30°$ adlayer), no aggregation into large islands is observed (Fig. 4.4 d-f). Despite the low temperature, only small aggregates of molecules form, with almost every molecule being accessible on the surface from at least one side (see Fig. 4.4d-f). This is, again, in marked contrast to CO films on extended terraces, where

extended ($\sqrt{3} \times \sqrt{3}$)R30° islands are found under similar conditions.[119] The distribution of molecules within the exposed facet is relatively featureless; no preferred or avoided regions of adsites can be discerned (Fig. 4.8).

## 4.4 Summary

A survey of the effects that nanometer-scale confinement can have on adsorbate dynamics and placement is conducted; on small exposed facets adsorbate diffusion increases rather than decreases, resulting in more even and open distributions of adsorbates and adlayer vacancies than found on extended terraces. Even at full coverage, confinement can stabilize dislocation lines that affect a substantial fraction of the molecules in the adlayer (more than one-fourth of them). In combination, these findings suggest that confinement alone can increase the potential for surface reactivity in an adsorbate film: the smaller the facet size (i.e., the smaller a metal nanoparticle that creates it), the more pronounced the mentioned effect.

# 5 Molecular Self-Assembly of Pinwheel Structures

This chapter is adapted from publication *Coalescence of 3-phenyl-propynenitrile on Cu(111) into interlocking pinwheel chains.* Volume 135, Issue 13, 2011 Journal of Chemical Physics.

The adsorption and subsequent self-assembly of molecules at metal surfaces provides a means of pattern formation on a length scale that has seen significant increases over the past decade;[2,12,121] originating at the sub-nanometer scale of individual small molecules,[105] it now reaches all the way to the ten nanometer scale connecting (almost) seamlessly to the feature size accessible via e-beam lithographic techniques. In this quest for methods capable of patterning surfaces on an uninterrupted length scale, the importance of intermolecular and substrate-mediated interactions in ordering adsorbate layers beyond the scale of their constituent molecules has become obvious.[5,15,122,123] Intermolecular interactions are generally roughly categorized into the formation of intermolecular hydrogen bonds,[5,24,124,125] the formation of metal coordination networks[28,53,122,126,127] and, in particular cases, covalent bond formation between adjacent species.[128-132] Substrate mediated interactions frequently involve the surface state of coinage metals or other electronic properties of the substrate.[87,133-137]

In this chapter, arrays of interlocking pinwheels composed of self-assembled phenyl- propynenitrile molecules, generated by a combination of hydrogen bonding

and substrate-mediated interactions - tentatively attributed to surface stress - will be discussed.

## 5.1 3-Phenyl-Propynenitrile Molecule

This study addresses 3-phenyl-propynenitrile (PPN), a carbon-carbon triple-bond acetylene group carrying on one end a cyano group and on the other a benzene ring (Fig. 5.1). Species without the nitrile group have been investigated by the White group,[138,139] where the surface binding has been ascribed to interaction of the acetylene with the substrate via a double-σ bridge-bonded acetylene. Calculations involving only two substrate atoms suggested that the aromatic moiety points away from the substrate. In the theoretical work, a global energy minimum for such a configuration is found; however, a secondary minimum for the aromatic ring and the cyano group close to the surface is additionally obtained. This result is in much better correspondence with the STM images obtained and, arguably, also more intuitive as there is no obvious reason for the benzene ring to avoid interaction with the substrate charge density. A similar pattern has also been predicted by White's group absent of theoretical affirmation.[139]

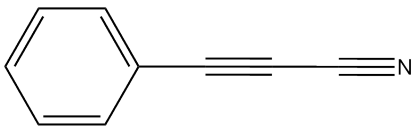


**Fig. 5.1** Chemical structure of 3-phenyl-propynenitrile (PPN) molecule

A number of publications reported on interactions between nitrile groups and adsorbed benzene rings, characterizing them as hydrogen bonding.[24,124,127,140] While in the solution phase, hydrogen atoms attached to aromatic rings are insignificant hydrogen bond donors,[141] at the liquid nitrogen temperatures accessed in this study - and including the possibility for donation of charge density to the ring from the substrate - they have been found to be pattern-determining.[15,125] This study will show, however, that this interaction by itself does not account for the pinwheel chains observed.

This chapter focuses on the coexistence of two PPN patterns on Cu(111): six-petal flowers and interlocking pinwheels, both at 3 molecules per 49 substrate atoms (resulting in a coverage of 6% of a monolayer), and the cause for the aggregation of seven flowers into a single pinwheel. The seamless and commensurate coexistence of these phases is noteworthy and will be discussed. At higher coverage a plethora of other structures were observed, in which the molecules arrange more densely, in agreement with Sohn et al.'s results.[138,139] Their multitude prevented us from understanding them in detail.

This study is carried out by a combination of STM imaging and DFT modeling of molecular adsorption structures. All STM measurements proceeded on sputter-and-anneal cleaned samples Cu(111), on which PPN was deposited at cryogenic temperatures (~100K) followed by annealing to room temperature for ~1 h; prior to annealing no stable imaging conditions were achieved. The resultant low

coverages leave roughly 2/3 of the surface area unoccupied. PPN was obtained commercially from Aldrich.

Density functional theory calculations, carried out by E. Chu, J. Wyrick, D. Salib, C. Holzke, and K. D. Cohen, use the VASP code[142] with the PW92 generalized-gradient approximation[143] for the exchange-correlation functional and projected augmented waves (for calculation of PPN adsorption geometries, the results were also verified with the plane-wave pseudopotential method[144] using ultrasoft pseudopotentials[145]). An electronic energy cutoff of 400eV and augmentation charge cutoffs of 640-700 eV were used. Since adsorption energy (differences) exceeded 1 eV, no Van der Waals interactions have been considered. All supercells use three substrate atomic layers and sufficient lateral space to prevent direct intermolecular interaction across the supercell boundary. A single *k* point was used in each cell, with the exception of the data of Fig. 5.10b, which uses three *k* points. All results are optimized so that the remaining forces are less than 0.04 eV/Å. W. Lu also performed TPD measurements, which agree with Sohn et al.'s data on phenylpropyne[138,139] and are not shown here.

## 5.2 Flower and Pinwheel Structures

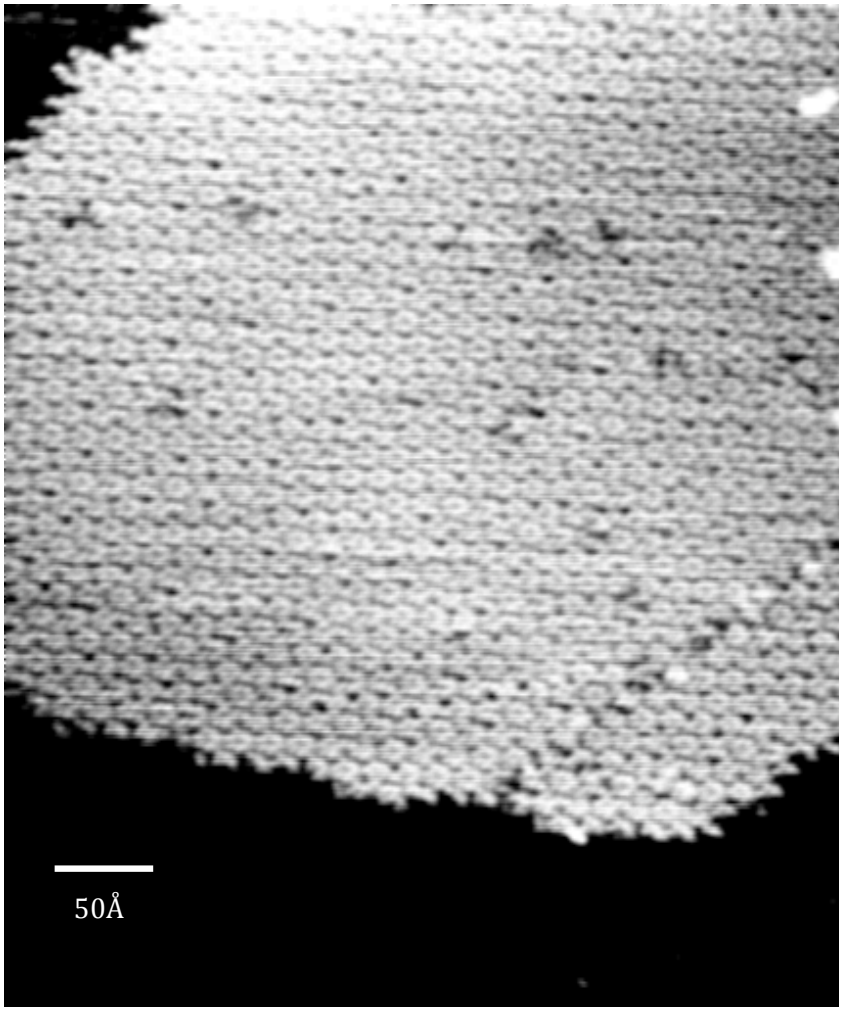


**Fig. 5.2** STM images of large islands of PPN on a Cu(111) terrace with a mixture of pinwheel and flower coverage. The top right corner shows a dislocation line in the island. Image parameters: bias, -1.3 V; current, 0.96 nA.

Fig. 5.2 shows STM images of a molecular islands of PPN on a Cu(111) surface exhibiting the coexistence between a pinwheel and a flower phase. The islands into

which the molecules aggregate are surrounded by empty terrace area, indicating that attractive intermolecular (or substrate mediated) interactions are at play. All such islands are found attached to the lower part of copper step edges, suggesting that the latter serve as nucleation points. Only some terraces contain molecular islands while others appear devoid of adsorbates, indicating that during room-temperature annealing molecules are able to cross step edges. Individual molecules are mobile on Cu(111) even at liquid nitrogen temperatures; however they are sufficiently slow to be observed during their diffusion to join molecular islands.

The molecular population of Fig. 5.3 consists of triplets of molecules forming a six-petal flower and heptamers of such flowers whose peripheral molecules are rearranged to form interlocking pinwheels. The flowers and pinwheels are lightly colored yellow and green, respectively, to facilitate their recognition. Approximately 2/3 of all molecules are part of pinwheels, 1/3 are not. On many images analyzed, a flower-covered area between pinwheels that is sufficiently large to accommodate another pinwheel is barely ever found. Rather, it appears as if the flower-covered area represents the interstitial space after coalescence of flowers into percolating pinwheel chains. The pinwheels interlock geometrically and, thus, form 'gear chains'; as each pinwheel owes its stability to the interplay between adsorbate-substrate and intermolecular interactions these 'gear chains' are not expected to be able to transmit rotation in any meaningful manner. The percolating nature of the pinwheels suggests that they formed sequentially; the presence of the flower phase

in the interstitial area indicates that, once formed, the pinwheel chains are relatively rigid and stable.

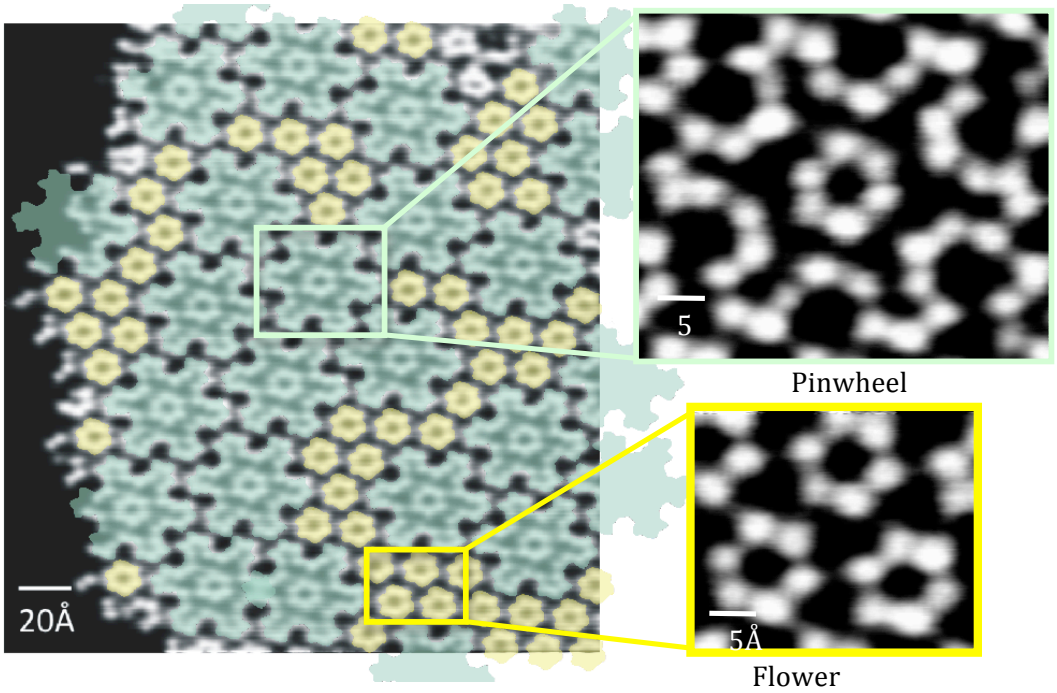


**Fig 5.3** Enlarged view of the coexisted pinwheel (colored green) and flower (colored yellow) structures. Image parameters: bias, -1.6 V; current, 80 pA.

Overlaying a grid on the molecular patterns (Fig. 5.4), it is found that both the flowers and the pinwheels' teeth and cogs lie on a hexagonal lattice and in registry with each other. The flowers form a (7×7)R23° pattern, which may also be described as a $\begin{pmatrix} 8 & -3 \\ 3 & 5 \end{pmatrix}$ pattern; the pinwheels form a (√7×√7)R19° superstructure of the flower pattern, which is a ($7^{3/2}$×$7^{3/2}$)R3° pattern or, in matrix notation, a $\begin{pmatrix} 19 & -1 \\ 1 & 18 \end{pmatrix}$ pattern. Its unit vectors are 47 Å long, its area is 1115 Å$^2$, and it contains 21 identical

molecules. While complex patterns of identical molecules have been found in many adsorption systems, 21 molecules per unit cell rank among the most complex molecular patterns.[15,53,124,146-148]

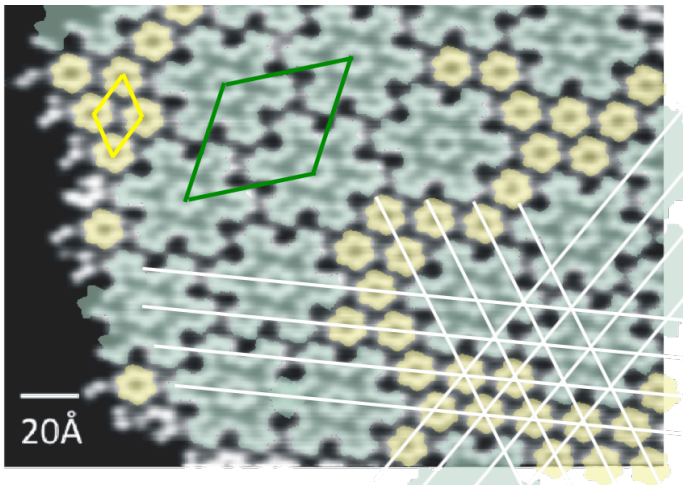


**Fig. 5.4** High symmetry directions of the adlayer are indicated. Both the flowers and the pinwheels' teeth and cogs are in registry with each other. The flowers form a (7×7)R23° pattern (indicated by yellow rhombus), and pinwheels form a $(7^{3/2}\times7^{3/2})$R3° pattern (green rhombus).

DFT modeling of the adsorption of the molecule on a 6×4×3 substrate atom supercell, as performed by E. Chu, results in an adsorption configuration shown in Fig. 5.5b. This configuration is in good agreement with Sohn et al.'s results on a similar species without the nitrile group for a substrate represented by two atoms only.[138]

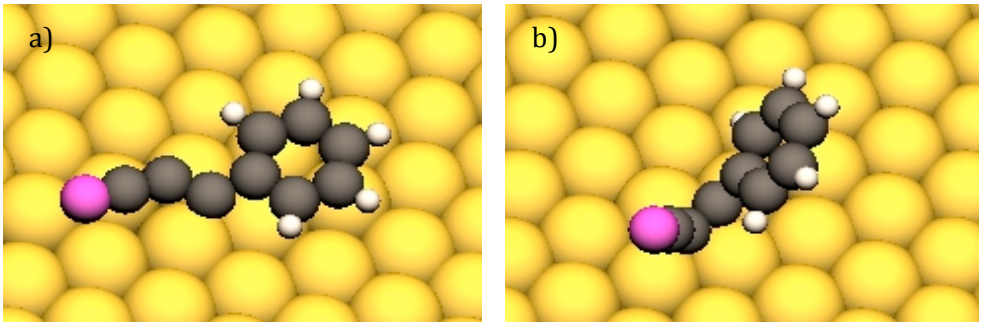


**Fig. 5.5** (a) The PPN configuration of a local minimum in the optimization. (b) The PPN configuration on Cu(111) that has the highest binding energy according to the calculations carried out by E. Chu.

In addition, it is found that - at substantially lower total adsorption energy (~1.5eV) - a second stable adsorption configuration (minimized to forces < 20 meV/Å), in which both the ring system and the cyano group rest nearly flat on the substrate (Fig. 5.5a), in significantly better apparent agreement with the elongated shape of the molecular units in STM (see for instances the edges of the island in Fig. 5.2 and Fig. 5.3). In this configuration the cyano group and the benzene rings are nearly coplanar, which allows lateral interaction between the molecules to be discussed in the following section. In both cases, the molecule is primarily attached to the substrate by insertion of the carbon-carbon triple bond into a substrate bridge, in good agreement with Sohn et al.'s results.[138,139]

## 5.3 Discussion

In this section I propose an adsorption model for the flower and pinwheel structures, based on which I will explain the coalescence of the flower structures

into pinwheels. These models rely on the adsorption configuration of PPN shown in (Fig. 5.5a), which is in much better geometric agreement with the STM images. In previous investigations of aromatic moieties pinned by reactive groups to metal surfaces,[125,149-151] it is generally found that the aromatic moiety comes to rest relatively close to the substrate, potentially providing some support for this configuration. While DFT codes quite consistently place aromatic species relatively far away from a metallic substrate,[152-155] experimental evidence, such as from standing wave x-ray absorption,[156] suggest a different behavior. Arguably, chemical intuition may also favor an adsorption configuration in which both the cyano and phenyl group are sufficiently close to the substrate for interaction rather than pointing away from it foregoing the opportunity of any interaction.

This adsorption configuration allows interpretation of the flower shapes as trimers of PPN molecules, in which the cyano nitrogen atom interacts with the hydrogen atom at the meta position of the phenyl ring (Fig. 5.6). Such an interaction is in good agreement with, for instance, the interactions found in benzenethiol films.[125,157] Aromatic hydrogen atoms have been found to form hydrogen bonds to nitriles and other nitrogen atoms in other organic groups quite frequently, further supporting this interpretation.[24,124,127,140] The experimental resolution is insufficient to distinguish reliably between the cyano and phenyl end of the molecule. Hence, it is unknown whether the film consists of trimers exclusively of one rotational orientation (enantiomer) or a (potentially ordered) racemic mixture of them.

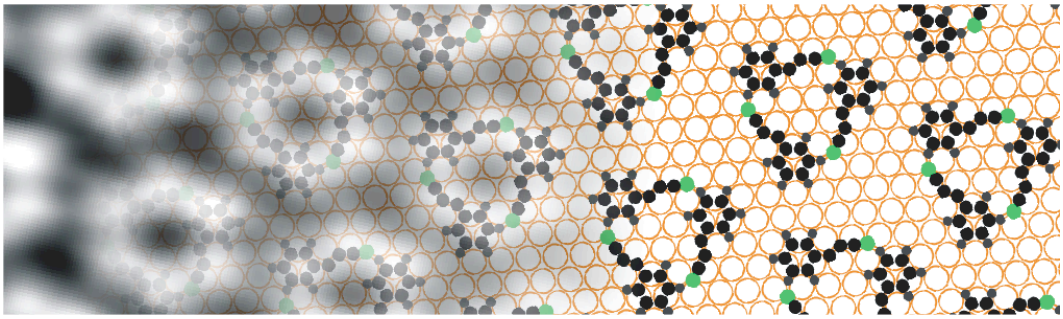

**Fig. 5.6** STM image of the flower phase and corresponding model based on the adsorbate configuration shown in Fig. 5.5 (a). Image parameters: bias: -1.5 V, current: 0.12 nA.

Starting out from this intermolecular interaction motif, a pinwheel structure that shows good agreement with the experimentally observed features can be constructed (Fig. 5.7). While the flower required only three rotational configurations of PPN on the substrate, the pinwheel requires six, as well as their inversion symmetric counterparts. Thus, while in the flower shape all molecules adsorb at equivalent sites (due to the threefold symmetry of the substrate), for the pinwheel structure the molecule needs to be inverted, corresponding to a change between hcp and fcc hollow sites.

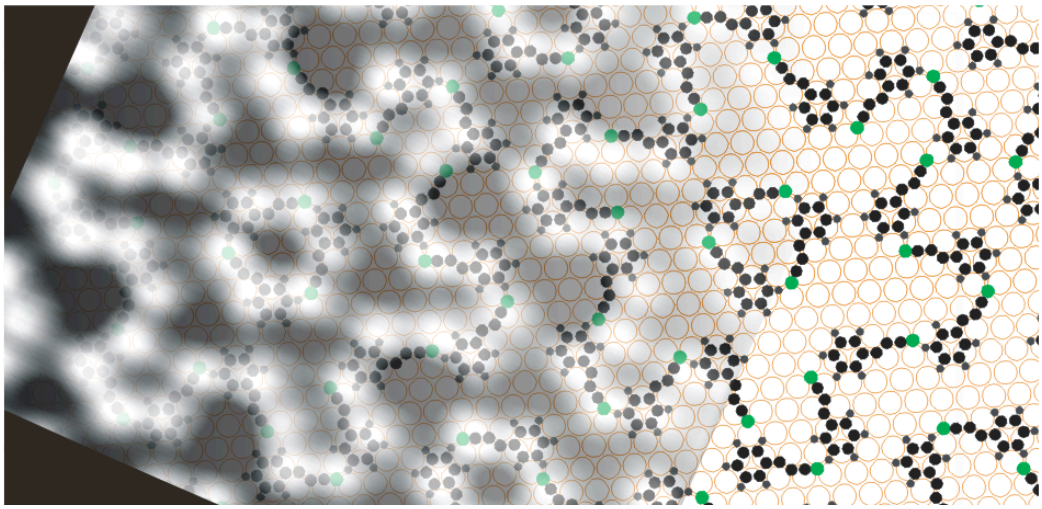

**Fig 5.7** STM image of the pinwheel phase and corresponding model. Image parameters: bias: -1.5 V, current: 0.12 nA.

There is no readily apparent energetic benefit in the formation of the larger, more complicated and, hence, entropically disfavored pinwheel structure from the perspective of direct intermolecular interaction: while there are slight variations between the intermolecular orientations in the pinwheel as compared to the flower pattern, if their energetic benefit would be substantial, a directly periodic arrangement of thus interacting species would be expected, rather than the kind of coalescence of the flowers into larger superstructures observed here. As the molecular patterns form on partially covered terraces, their molecular adlayer is not subjected to compressive stress or strain. Consequently, a different origin of this phenomenon is expected.

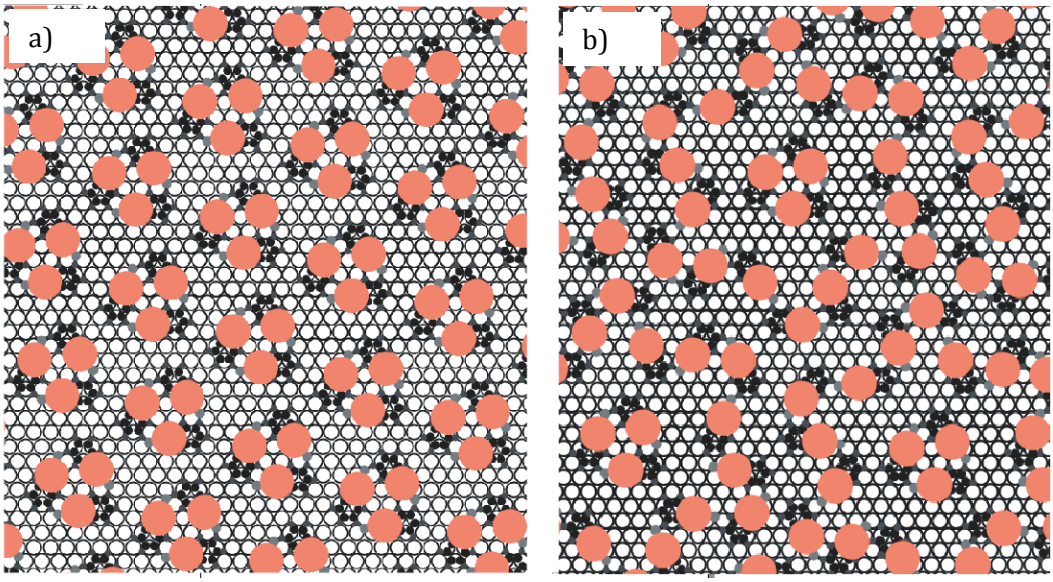


**Fig. 5.8** Spatial distribution the acetylene groups in the (a) flower and (b) the pinwheel structure. In the flower pattern the acetylene species are bunched more frequently in close trimers, although the overall coverage is identical to the pinwheel structure.

A close inspection of the primary interaction of PPN with the substrate suggests that the insertion of the acetylene group into a substrate atomic bridge will create expansive stress in the top substrate layer. Could this stress be the origin of the formation of the pinwheels? To substantiate this, Fig. 5.8 shows the flower and the pinwheel pattern, highlighting the locations at which the acetylene group inserts itself into a substrate atomic bridge: in the flower pattern, closely spaced triplets of this interaction are distributed on a regular hexagonal network. While at the center of a pinwheel the same triplet is found, the six peripheral locations in the pinwheel

appear to distribute their 18 acetylene moieties more evenly (as opposed to clustering them in six triplets on a regular hexagonal grid).

To evaluate this quantitatively, the spatial correlation between the acetylene moiety locations $\boldsymbol{x}$ in one pinwheel unit cell and the acetylene moiety locations in the same unit cell as well as the six surrounding unit cells (i.e. a total of $\underset{\text{acetylene moieties in pinwheel}}{(3\times7)} \times \underset{\text{self and surrounding pinwheels}}{7(3\times7)} - \underset{\text{self-correlation}}{(3\times7)}$ = 3066 distances $r$) is calculated. The same correlation for the flower pattern in the same area is also calculated. Assuming for simplicity that the relaxation of the substrate stress is proportional to the distance from the stress center (i.e. a $1/r$ potential), the sum $s$ over the reciprocal of all distances is about 0.4 percent smaller for the pinwheel structure than for the flower structure.

$$s = \sum_{i}^{\text{Acetylene moieties in center PW}} \sum_{j}^{\text{Acetylene moieties in 7 PWs}} \frac{1}{\left|\vec{x}_i - \vec{x}_j\right|}$$

Clearly, a perfect 1/distance dependence of the stress potential is an oversimplified assumption. However, a higher power would only increase the reduction of strain energy (e.g. a $1/r^2$ relationship leads to 2.4 percent) and a lower power (i.e. an even longer range potential) would be hard to justify.

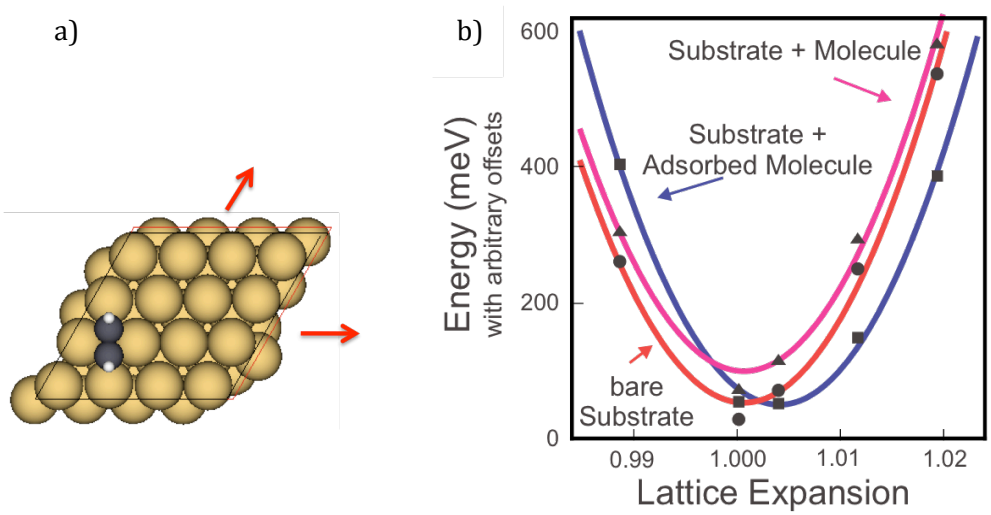


**Fig. 5.9** (a) Schematic show of the DFT modeling approach by expanding the Cu(111) lattice in two basic lattice directions. (b) shows the dependence of the total energy of a (circle) 6×4×3 Cu slab, (triangle) Cu slab with a non-adsorbed acetylene molecule and (squares) a Cu slab with an adsorbed acetylene molecule, on the copper lattice constant. The larger equilibrium energy indicates expansive stress induced by the di-σ interaction of PPN acetylene moiety with the substrate.

Direct DFT modeling of these long-range interactions requires too large of a supercell to be feasible. However, the presence of expansive stress caused by adsorption of an acetylene group on the substrate can be corroborated: to this end, J. Wyrick, C. Holzke, D. Salib, and K. D. Conhen calculate the total energy of a 6×4×3 substrate atoms supercell with no acetylene molecule attached, with an acetylene molecule in the vacuum above the substrate, and with the acetylene chemisorbed on the surface. Varying the geometric dimensions of the supercell to cause slightly

larger or smaller lateral interatomic spacing of the copper atoms (Fig. 5.9) while maintaining constant overall cell volume (through variation of the amount of vacuum separating the slabs), they find that the lowest energy is found at smaller lateral Cu spacing in the first two cases and at larger one in the last case. This clearly demonstrates that the kind of interaction found between PPN and the substrate exert stress to expand the substrate lattice.

## 5.4 Conclusion

3-phenyl-propynenitrile (PPN) on Cu(111) forms a hexagonal network of molecular trimers, which coalesce into sequences (gear chains) of interlocking pinwheel-shaped heptamers. Density functional theory modeling of the adsorption of individual molecules results in two adsorption configurations, of which the one with the lower calculated binding energy appears to be the physically correct solution, representing a near-planar molecule in close proximity to the substrate. Evaluation of the lateral distribution of molecule substrate interaction centers suggests relief of adsorption-induced surface strain as the driving force behind the formation of the large pinwheel structures.

# 6 Metal-Organic Coordination on a 2D Surface

Over the past decade metal atom coordination at metal surfaces has emerged as a technique that permits the formation of a range of supramolecular structures in a size region that bridges the angstrom scale of conventional adsorbate patterns and the tens of nanometers scale of high-end lithography.

The resultant patterns and networks consist of molecules bound to and arranged around metal adatoms.[16,27,28,122,130,158-166] Coordination assemblies with various ligand molecules and different metal centers have been reported, including molecules with functional groups such as thiol[167-170], pyridyl[10,126,171-178], cyano[9,13,16,18,53,127,179-184], isocyano[8,185], aldehyde[16], and carboxyl[10,14,27,28,160,163,176-178,186-192], and metal centers such as Co[9,13,16,18,181,182], Ni[53,180,193], Mn[180,184,186,187], Fe[10,14,16,53,160,163,173,178,188,190,191], Au[8,168-170,179,185], and Cu[27,28,126,127,167,171,172,174-177,183,189,192,194] atoms with 2-fold[8,10,53,168-172,174,185,189,195], 3-fold[9,13,16,18,127,179,191], or 4-fold[28,163,180,184,190,191] coordination on different surfaces including Cu(100)[10,14,16,28,126,160,163,176-178,184,188,190,191], Cu(110)[27,189], Cu(111)[127,167,171,174,182,183,192,194], Ag(100)[126,180], Ag(111)[9,13,16,18,126,182], Au(111)[8,168-170,172,173,179,181,185-187,193], and NaCl bilayer coated Cu(111)[53]. They generate networks with a variety of geometries including hexagonal[9,13,16,18,167], rhombic[172,173], rectangular[10,14,160,167,178,186,187,190,193], square[14,126,160,163,176,184,190,194], Kagome[173], six-star[18], and linear chain, [8,27,168,174,175,185,194] or random chain[181,182] structures as well as isolated coordinated molecular pairs[53,168,170,171,174,183,189,192], triangles[174],

rhombi[174], pentagons[174], hexagons[174], etc. have also been reported. The adatoms can either be extracted from the substrate,[28,127,177] or more commonly originate from a dedicated deposition step. The latter procedure can provide adatom species different from the substrate material.

Coordination chemistry generates relatively rigid and strong bonds involving bond energies on the order of 1 eV, i.e. roughly an order of magnitude stronger than hydrogen bonds or dipolar interactions at metal surfaces.[127] Their strength is generally sufficient to supersede all other adsorbate-substrate interactions. Identical patterns have been prepared on substrates of different symmetry and chemical identity.[126] Variation of the length of the ligands can scale the pores size of the coordination network,[122] which offers exciting opportunities for the fabrication of tailored templates for subsequent deposition steps.[4,115,196] Using a binary mixture of molecules, ordered lattices that incorporate both species in addition to the coordination centers have been prepared.[10]

In solution, ligands play a role in determining the most favorable coordination geometries in addition to stabilizing the charge, if any, on the coordination center. For example, both $Ni(pyridine)_4(BF_4)_2$ and $K_2NiCl_4$ have oxidation state +II,[197] but they display square planar and tetrahedral geometries, respectively, due to the donor properties of the different ligands.

In contrast, at a surface, the adatom is not free to assume any coordination geometry, as the interactions between adatom and surface must be considered. At

maximum a half-sphere is available for coordination bonds, with the lower half-sphere occupied by the substrate. Enforced by the interaction between the ligands and the underlying substrate, planar geometries are usually observed. Moreover, at a surface the conventional definition of oxidation state is not directly applicable, because the substrate may donate charge to the center. The orbital configuration of a center is also not well definable, at least with regards to the substrate-side half sphere, which is more commonly described by density functional theory modeling of the embedding of the adatom into the substrate charge density than by any model involving particular bonds.

Nevertheless, studies on surface coordination have shown that particular combinations of adatom, substrate and ligand result in a particular coordination geometry. While there are many examples in which the symmetry of the surface (e.g. 2-fold for fcc(110), 3-fold for fcc(111), 4-fold for fcc(100)) matches the coordination geometry of coordination compounds, there are also as many examples to the contrary. This indicates that for the half sphere not covered by the substrate, where coordination with ligands occurs, a description based on orbital geometry may be possible, helpful in creating an intuitive and descriptive understanding of surface coordination chemistry and predictive for the design of surface coordination compounds.

In this chapter, recent works on cyanide and isocyanide molecules relating to metal-organic coordination interactions are discussed. Previous studies of 1,4-

diisocyanobenzene by W.T. Tysoe and coworkers found that the isocyano group is very reactive in forming metal-organic coordination bonds on metal surfaces. They also highlighted the catalytic activity of the unsaturated bonded central metal atoms. Yet most features and properties are still in blank. The study in this chapter is to explore the bond features by a comparative study of isocyanide and cyanide molecules with the same molecular backbone.

All STM measurements are taken at liquid nitrogen temperature (~85K). Molecules are sublimed from a line-of-sight glass tube, to a sputter-and-anneal prepared Cu(111) substrate held at ~100K. The sample is subsequently annealed to 298K, at which temperature Cu adatoms can "evaporate" from the step edges of the copper substrate, and thus become available to form metal-organic coordination compounds.

## 6.1 Diisocyanoanthracene Molecule

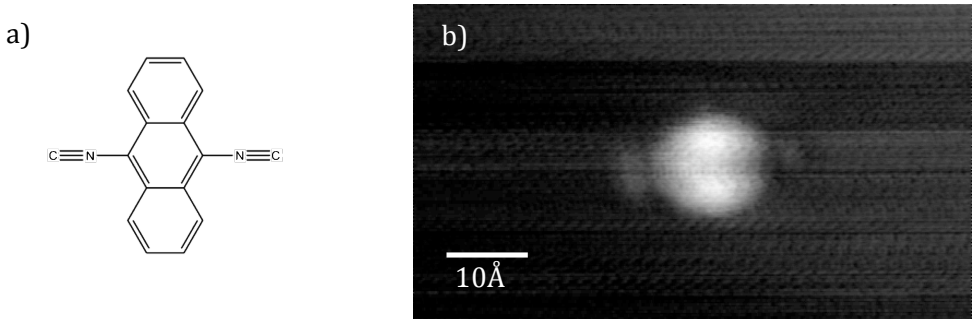


**Fig. 6.1** (a) Chemical structure of 9,10-diisocyanoanthracene (DICA); (b) STM image of an isolated DICA molecule on Cu(111). Image parameters, 7nm × 4nm; bias, -1.5 V; current, 88 pA.

The 9,10-diisocyanoanthracene (DICA) has an anthracene molecular backbone, with the isocyano group as the legs on each side (Fig. 6.1a). In STM images, the anthracene moiety appears as bright protrusions, and the isocyano legs appear as faint shoulders (Fig. 6.1b).

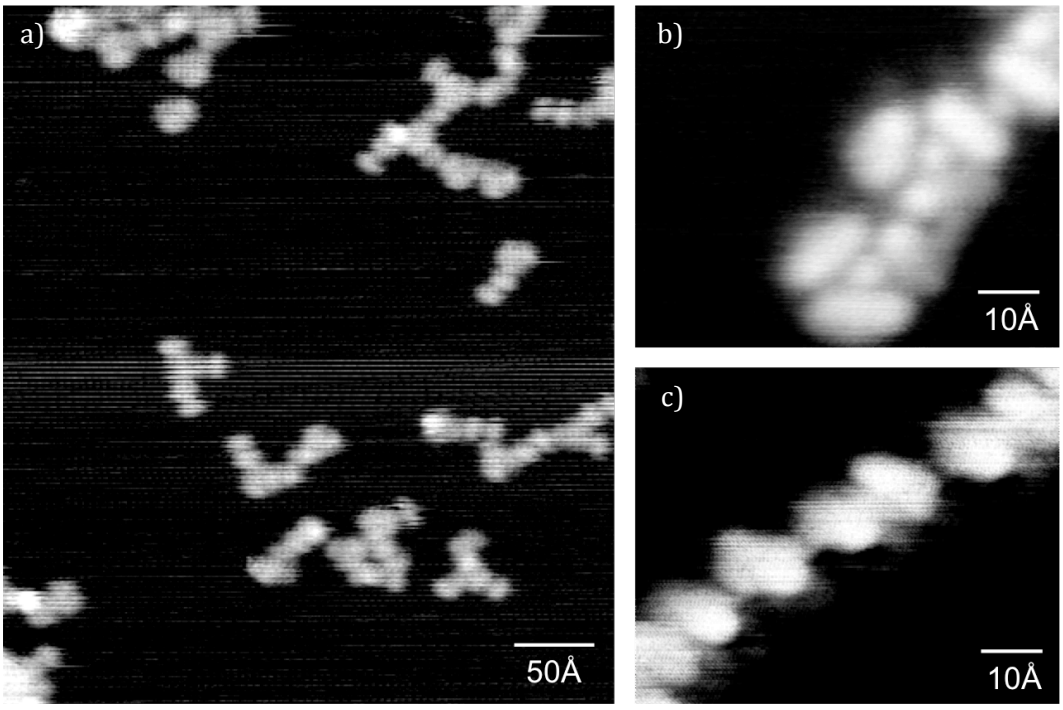


**Fig. 6.2** STM images of Cu-DICA coordination structures on Cu(111). (a) shows an overview for coordinated structures of low coverage. (b) and (c) are the zoomed in images for the nodal motif and chain motif, respectively. Image parameters: (a) bias, -1.5V; current, 78pA. (b) bias, -2.10V; current, 0.12nA. (c) bias, -1.3V; current, 93pA

The molecules orient along the [1-10] direction of the Cu(111) surface, and do not aggregate into large islands after coordinating with Cu adatoms at low molecule

coverage (Fig. 6.2a). Two bonding motifs show up for the coordinated structures: triangle and short chain. The triangles are composed of three DICA molecules coordinating to a Cu atom, which appears as a protrusion in the center of each triangle (Fig. 6.3a). The short chains pose a ~30° angle with the principle directions on the Cu(111) surface. Notably the molecules are separated with a non-equal distance in the chain structure. More specifically, they have longer and shorter separation alternatingly, as shown in Fig 6.2c and Fig 6.4. The center-to-center distance between molecules within a pair is 9Å, and that for the adjacent pairs is 20Å.

Based on the separation distances and orientations of the molecules, models for the triangle and chain structures are proposed. The triangle structure can result from a 3-fold coordination of a central Cu atom bonded to three DICA molecules, with the central Cu atom sitting at a hollow site and the molecules orienting along the principal directions (Fig. 6.3a). This agrees well with a previous study on Cu coordination with dicyanoanthracene (DCA) molecules – a molecule that is almost identical to the DICA studied here, except for the isocyano group replaced by the cyano functional group in the DCA case.

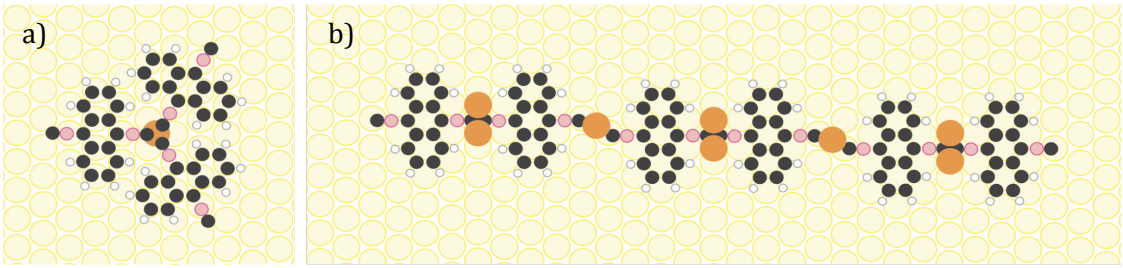


**Fig. 6.3** Proposed model for triangle motif (a) and chain motif (b).

The chain structure is somewhat more complex. As shown in Fig. 6.3b, the bond between molecules within pairs can be coordination involving two Cu atoms, while adjacent pairs are connected by coordination involving one Cu atom. Each pair is offset perpendicular to the row direction by ½ of a Cu atomic distance. This model agrees very well with the observed separations between molecules as well as the chain orientations. In addition, all coordinated Cu atoms in the chain structure are sitting at bridge sites on the Cu(111) substrate, which are expected to be stable which isonitrile coordinate.

Random network structures appear at a higher DICA coverage, with the chain and triangle motifs serving as linkers and nodes, respectively (Fig. 6.4). In addition, the population of molecules involved in the chain motif exceeds that for the triangle, indicating a more stable configuration for the chains.

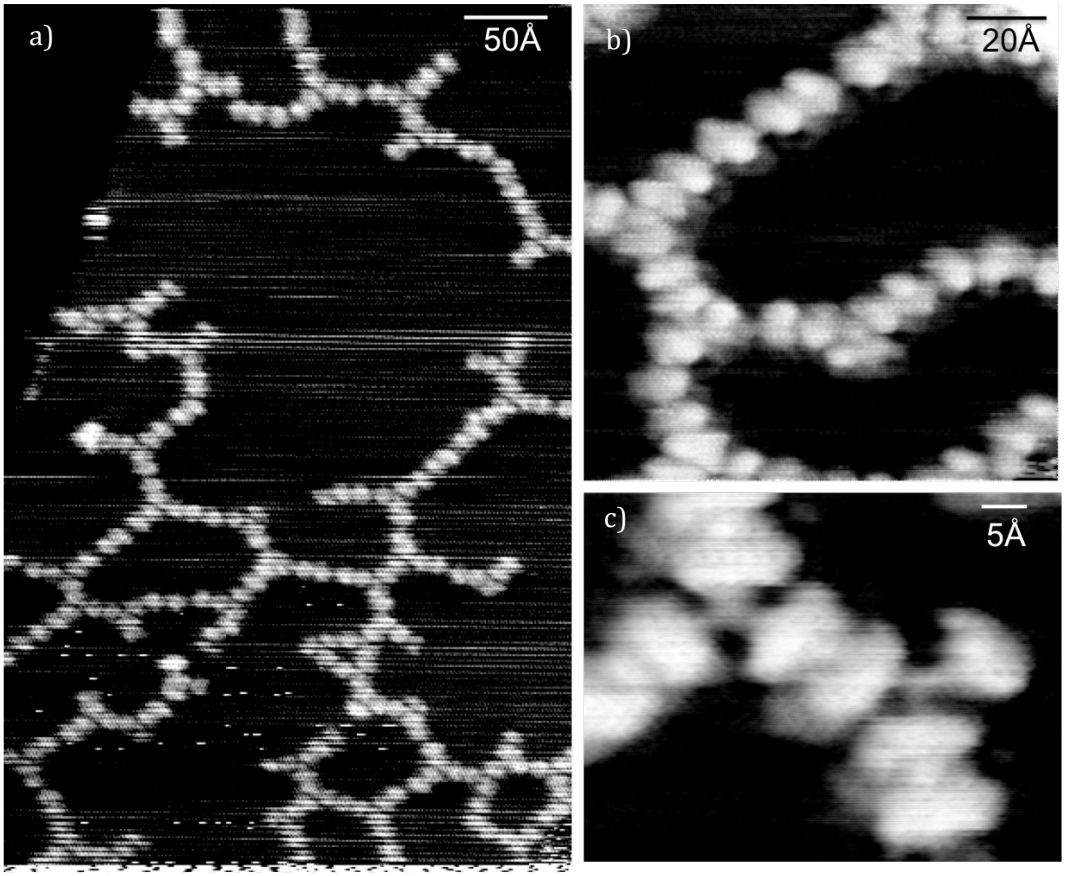


**Fig. 6.4** (a) Random network structures at a higher DICA coverage. (b) A close view of the network shows a random interconnection of nodal and chain motifs. (c) High resolution image at the connections. Image parameters: (a) bias, 1.3V; current, 81pA. (b) bias, -1.3V; current, 93pA. (c) bias, -1.3V; current, 76pA.

Occasionally, a curled chain structure is observed. Instead of forming a linear-looking chain with molecules paired up, this curled chain is formed by DICA and Cu atoms bonded to each other sequentially with a 1:1 ratio, as indicated by the STM image (Fig. 6.5a). Apparently not all DICA molecules are lying along the principal

directions, revealing that the coordination is capable to sustain distortions without breaking the bond. A “flip” of one end of the short chain is observed (Fig. 6.5). This can result from a mismatch between the curled chain structure and the registry of substrate, making the chain flickering from one meta-stable configuration to another.

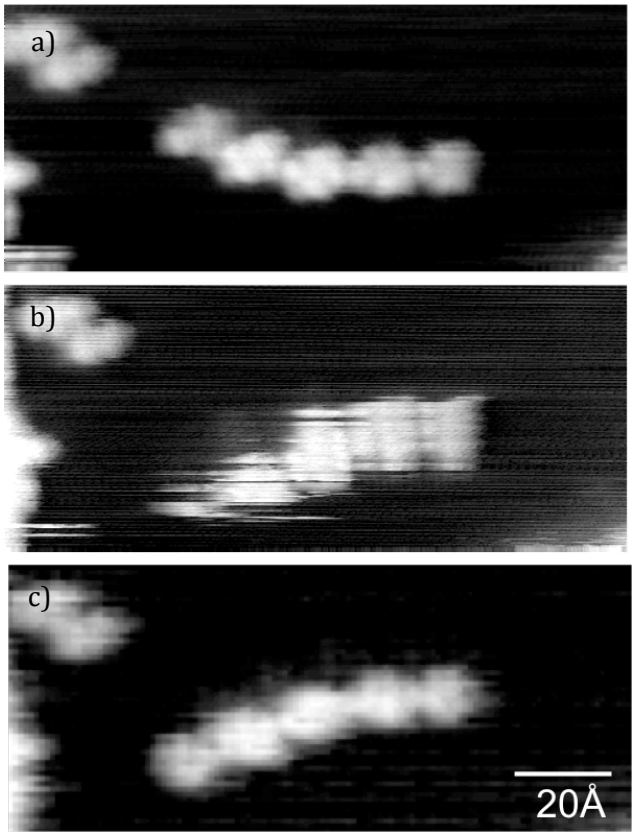


**Fig. 6.5** Sequential STM images of a curled chain structure. (a,c) the initial and final configuration of the “flickered” chain, and (b) is the imaged while the motion happens. Image parameters, bias, -1.5V; current, 88pA.

Compared to the coordination of a Cu atom by the DCA molecule, the isocyano group of DICA generates different features. Only 3-fold coordination is observed for the Cu-DCA system, while both chain and 3-fold triangle structures manifest themselves for the case of Cu-DICA, with the former motif dominates. Further more, although the 3-fold coordination motifs of these two molecules look similar in the local structure, they do behave differently at a larger scale. The 3-fold coordinated Cu-DCA interconnects into extended islands on the surface, while no long-range periodicity is observed for Cu-DICA coordination network, of which the 3-fold triangles connect to the chains and distribute randomly, glassy instead.

Different Cu coordination bonding feature between cyano and isocayno groups can be the origin of the different structures. The coordination between Cu atom and isocyano group can be stronger than that of cyano, since the carbon atom in the isocyano group is expected to donate electrons more willingly, thus making a stronger interaction with Cu. This can further affect the bond length, resulting a different structure to match the substrate registry. Further confirmation and explanation from theoretical calculation will be helpful.

## 6.2 Isocyanonaphthalene Molecule

The 2-isocyanonaphthalene (ICN) molecules are prepared and studied in a similar fashion. The ICN molecule has the isocyano group attached to an alpha position of the naphthalene backbone (Fig. 6.6a). Notably the asymmetric feature of

the ICN results in a racemic mixture of the molecules under the confinement of a 2-dimenional surface.

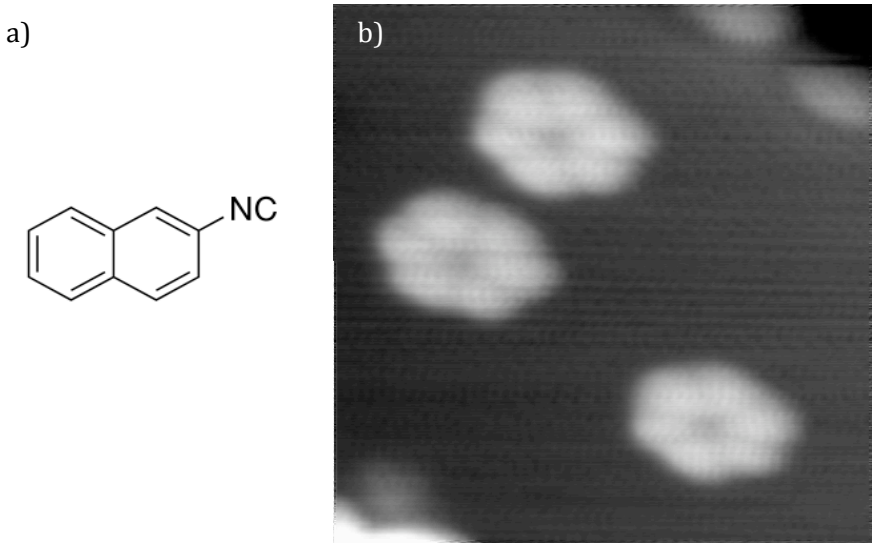


**Fig. 6.6** (a) Chemical structure of ICN molecule; (b) STM image of rotating ICN molecules on Cu(111) at 90K. The flower shape originates from the rotation of naphthalene moity around the isocyano group that anchors the substrate. Image parameter, 6.9 nm × 6.9 nm; bias, -1.6 V; current, 81 pA.

Six-petal flower shape protrusions are observed in STM images (Fig. 6.6b). They are identified as ICN molecules in a rotational motion. Breaking the status by applying electron pulses from the STM tip further confirmed this. The imaged flower-shape originates from an averaging effect of STM measurement when imaging molecules rotating much faster than the imaging speed (~min per image range). This is analogous to the observation of fast rotating blades of a mechanical fan with naked eye.

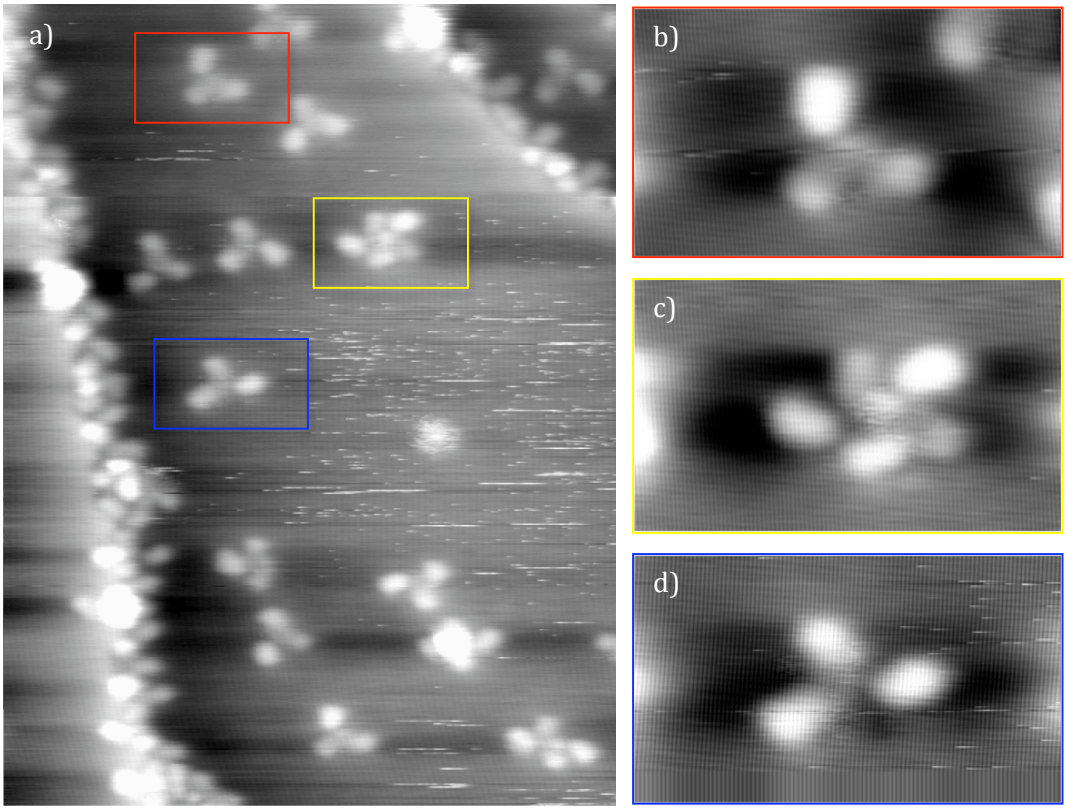


**Fig. 6.7** Coordination complexes of Cu-ICN on Cu(111). (b,c,d) are high resolution images of complexes in rectangles of (a). Image parameters: bias, -1.6V; current, 49pA; temperature, 40K.

Coordination compound of 3-, 4- and 5-molecule complexes appear on the Cu(111) surface after annealing the sample to 298K. (Fig. 6.7) Each 3- or 4-molecule complex can have one Cu atom coordinated in the center. The 5-molecule complex may involve two bonded Cu atoms, as indicated by its elongated shape. Different electronic structures of the central Cu atoms in different complexes are expected, and ongoing theoretical calculation will be very helpful in unveiling more detailed properties.

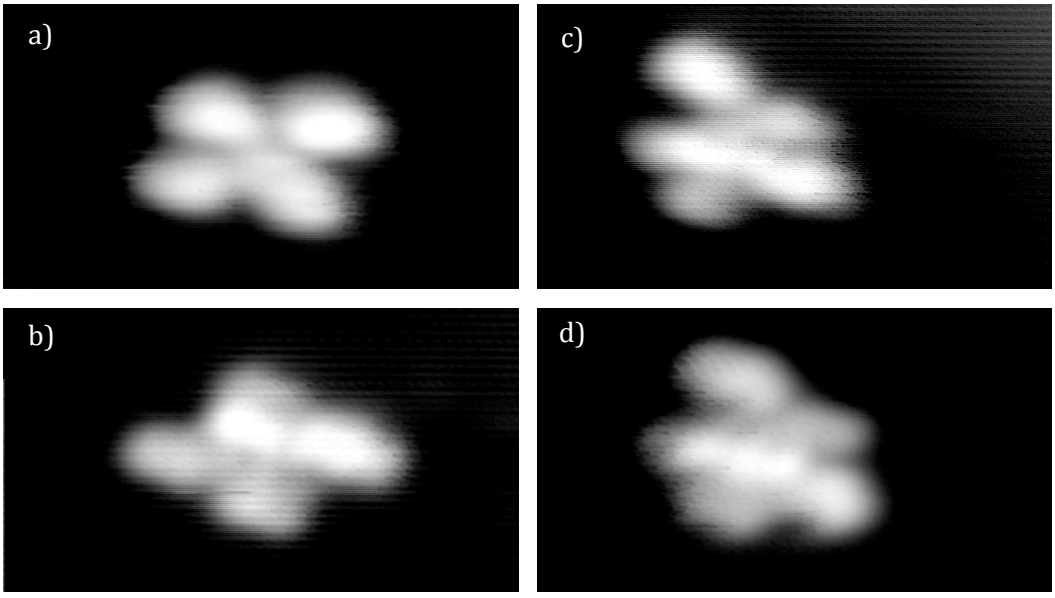


**Fig. 6.8** Different configurations of 4-molecule (a,b) and 5-molecule (c,d) complexes. The asymmetrical feature of the ICN molecules and 2-dimensional substrate confinement bring more complexity to the system. Image parameters, temperature, 90K. (a) bias, -1.9V; current, 74pA. (b) bias, -1.4V; current, 80pA. (c) bias, -1.2V; current, 80pA. (d) bias, -1.7V; current, 78pA.

In addition, there is a coexistence of different configurations for coordination complexes with the same number of molecules, as shown by Fig. 6.7bd for 3-molecule complexes and Fig 6.8 for 4- and 5-molecule complexes. This can be attributed to the chirality feature induced by confining the asymmetric ICN molecules in a 2D space. In other words, there are two different ICN species available on the surface, thus bringing more complexity to the configuration.

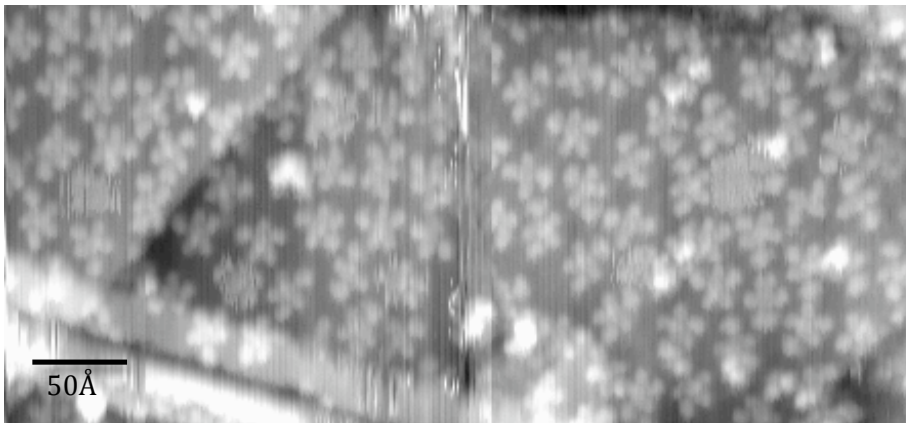


**Fig. 6.9** Coordination complexes prepared under high ICN dosage. 4- and 5-molecule complexes are present while the latter dominates. 3-molecule complexes are absent under this ICN coverage.

The 3-molecule complexes are common at low coverage, yet become absent when close to one monolayer, at which coverage the 5-molecule complexes occupy the major population of ICN molecules instead (Fig. 6.9). This implies a selectivity of the coordination compound formation as the molecule coverage varies.

## 6.3 Cyanonaphthalene Molecule

As a comparison, the molecule of 2-cyanonaphthalene (CN), with the same naphthalene backbone but a cyano group, is studied (Fig. 6.10a).

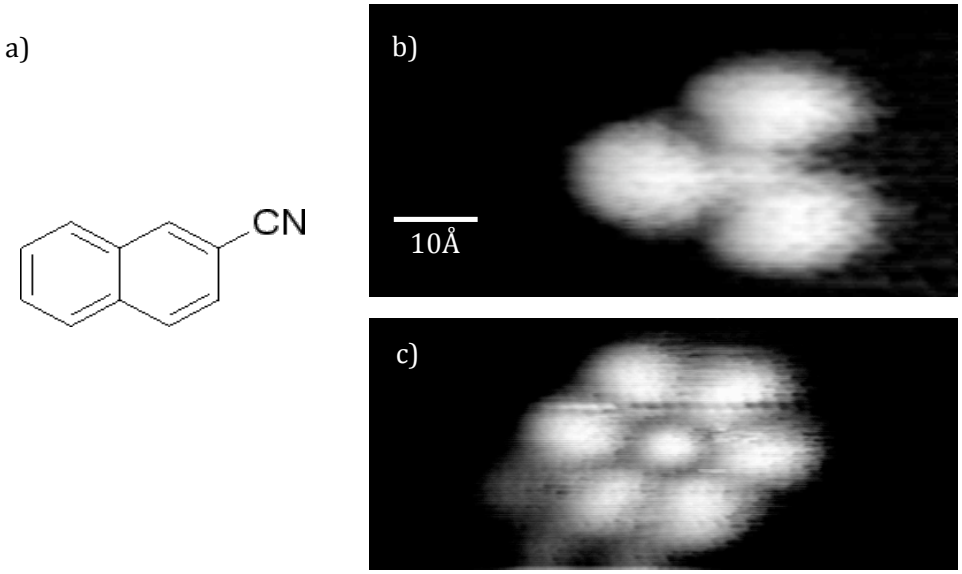


**Fig. 6.10** (a) Chemical structure of CN molecule. (b, c) 3-molecule and 6-molecule coordination complex on Cu(111). Image parameters, (b) bias, -2.1V; current, 48pA. (c) bias, -2.0V; current, 81pA.

The uncoordinated CN molecules are mobile on Cu(111) surface at 90K, and complexes with coordination numbers ranging from 3 to 6 appear after the sample annealed to 298K. The 3-molecule complex, as shown in Fig. 6.10b, can only be imaged with a very low tunneling current (~50pA). The large and fuzzy petals in the STM image indicate a hindered rotational motion for the bonded CN molecules within the complex. 6-molecule complexes (Fig. 6.10c) are unique for Cu-CN coordinated systems. The bond between Cu and cyano group is expected to be relatively labile compared to that for the isocyano group. This can result in a longer bond length, thus providing a larger space to accommodate as many as 6 molecules.

## 6.4 Summary

Metal-ligand coordination between Cu and isocyano/cyano fuctional groups on a Cu(111) surface have been studied with STM. Molecules with the same anthracene /naphthalene backbone but different functional group formed different coordination structures with Cu atoms. The differences can be mainly attributed to the different bond length and bonding energy. Theoretical modeling will be helpful to provide a more quantitative explanation on the configuration and bond features observed.

# 7 Future Work

Many interesting properties relating to the studied systems included in this dissertation can be further investigated.

## 7.1 Nano-Scale Confinement

The power of nano-scale confinement has been demonstrated to influence the spatial distribution and dynamic properties of small molecules enclosed. The cavities in anthraquinone network clearly exert guidance on CO's spatial distribution over a ~nm range distance. New strategy of manipulating small molecules may arise from applying similar confinement conditions. The influence of network cavities with different sizes and shapes can be investigated. The confinement effect on other small molecule such as $H_2O$ can also be explored in future studies.

The significantly reduced diffusion barrier of the confined CO molecules, and the persistent yet mobile dislocation line between CO domains implies a potentially higher reactivity of confined CO. Introducing other species such as $O_2$ into this system may permit further study of the reactivity.

## 7.2 Metal-Organic Coordination on 2D Surfaces

Metal-organic coordination on 2D surfaces is a relatively young field and has lots of exciting opportunities. Highly ordered and robust networks can be engineered, taking advantage of the directionality and large bond energy of metal-organic coordination. High catalytic activity can rise from the unsaturated bonded

metal atoms. Even novel nano devices may be designed, utilizing the metal centers bonded and stabilized by the surrounding ligand molecules. Numerous studies can be carried out relating to this area.

Support from theoretical calculation will be very helpful to provide a more detailed description of the properties on these metal-organic coordination compounds discussed in this dissertation.

In addition, the random networks formed by diisocyanoanthracene (DICA) molecules exhibit the feature of short-range order and long-range disorder. Statistical analysis on these structures may provide insights to the glassy state.

In the various coordination complexes formed by 2-isocyanonaphthalene (ICN) and 2-cyanonaphthalene (CN) molecules, different electronic structures are expected for the coordinated Cu atoms in different complexes. This can be characterized by further spectroscopic measurements. Applying other surface characterization techniques such as X-ray photoelectron spectroscopy (XPS) can also help in obtaining a more comprehensive understanding of their electronic characters.

# 8 REFERENCES


1 Kudernac, T., Lei, S. B., Elemans, J. A. A. W. & De Feyter, S. Two-dimensional supramolecular self-assembly: nanoporous networks on surfaces. *Chem Soc Rev* **38**, 402-421 (2009).

2 Barth, J. V. Fresh perspectives for surface coordination chemistry. *Surf Sci* **603**, 1533-1541 (2009).

3 Stohr, M., Wahl, M., Spillmann, H., Gade, L. H. & Jung, T. A. Lateral manipulation for the positioning of molecular guests within the confinements of a highly stable self-assembled organic surface network. *Small* **3**, 1336-1340 (2007).

4 Stepanow, S., Lin, N., Barth, J. V. & Kern, K. Non-covalent binding of fullerenes and biomolecules at surface-supported metallosupramolecular receptors. *Chem. Com.*, 2153-2155 (2006).

5 Theobald, J. A., Oxtoby, N. S., Phillips, M. A., Champness, N. R. & Beton, P. H. Controlling molecular deposition and layer structure with supramolecular surface assemblies. *Nature* **424**, 1029-1031 (2003).

6 Cheng, Z. H. *et al.* Adsorbates in a Box: Titration of Substrate Electronic States. *Phys Rev Lett* **105** (2010).

7 Lobo-Checa, J. *et al.* Band Formation from Coupled Quantum Dots Formed by a Nanoporous Network on a Copper Surface. *Science* **325**, 300-303 (2009).

8 Boscoboinik, J., Kestell, J., Garvey, M., Weinert, M. & Tysoe, W. T. Creation of Low-Coordination Gold Sites on Au(111) Surface by 1,4-phenylene Diisocyanide Adsorption. *Top Catal* **54**, 20-25 (2011).

9 Schlickum, U. *et al.* Metal-organic honeycomb nanomeshes with tunable cavity size. *Nano Lett* **7**, 3813-3817 (2007).

10 Langner, A. *et al.* Self-recognition and self-selection in multicomponent supramolecular coordination networks on surfaces. *P Natl Acad Sci USA* **104**, 17927-17930 (2007).

11 Barth, J. V. Molecular architectonic on metal surfaces. *Annu Rev Phys Chem* **58**, 375-407 (2007).

12 Bartels, L. Tailoring molecular layers at metal surfaces. *Nature Chemistry* **2**, 87-95 (2010).

13 Kuhne, D. *et al.* High-Quality 2D Metal-Organic Coordination Network Providing Giant Cavities within Mesoscale Domains. *J Am Chem Soc* **131**, 3881-+ (2009).

14 Stepanow, S., Lin, N., Barth, J. V. & Kern, K. Surface-template assembly of two-dimensional metal-organic coordination networks. *J Phys Chem B* **110**, 23472-23477 (2006).

15 Pawin, G., Wong, K. L., Kwon, K. Y. & Bartels, L. A homomolecular porous network at a Cu(111) surface. *Science* **313**, 961-962 (2006).

16 Stepanow, S. *et al.* Surface-assisted assembly of 2D metal-organic networks that exhibit unusual threefold coordination symmetry. *Angew Chem Int Edit* **46**, 710-713 (2007).
17 Luo, M. M. *et al.* Coalescence of 3-phenyl-propynenitrile on Cu(111) into interlocking pinwheel chains. *J Chem Phys* **135** (2011).
18 Schlickum, U. *et al.* Surface-Confined Metal-Organic Nanostructures from Co-Directed Assembly of Linear Terphenyl-dicarbonitrile Linkers on Ag(111). *J Phys Chem C* **114**, 15602-15606 (2010).
19 Somorjai, G. A. Introduction to surface chemistry and catalysis. *John Wiley & Sons, Inc.* (1994).
20 Ho, W. Single-molecule chemistry. *J Chem Phys* **117**, 11033-11061 (2002).
21 Wong, K. L., Rao, B. V., Pawin, G., Ulin-Avila, E. & Bartels, L. Coverage and nearest-neighbor dependence of adsorbate diffusion. *J Chem Phys* **123**, - (2005).
22 Bartels, L., Rao, B. V. & Liu, A. W. Translation and rotation of a haloaromatic thiol. *Chem Phys Lett* **385**, 36-39 (2004).
23 Patrick Han, P. S. W. Electronic substrate-mediated interactions. *Surf Sci Rep* **67**, 19-81 (2012).
24 Yokoyama, T., Yokoyama, S., Kamikado, T., Okuno, Y. & Mashiko, S. Selective assembly on a surface of supramolecular aggregates with controlled size and shape. *Nature* **413**, 619-621 (2001).
25 Lin, N., Stepanow, S., Ruben, M. & Barth, J. V. Surface-Confined Supramolecular Coordination Chemistry. *Top Curr Chem* **287**, 1-44 (2009).
26 Tseng, T. C. *et al.* Two-dimensional metal-organic coordination networks of Mn-7,7,8,8-tetracyanoquinodimethane assembled on Cu(100): Structural, electronic, and magnetic properties. *Phys Rev B* **80** (2009).
27 Classen, T. *et al.* Hydrogen and coordination bonding supramolecular structures of trimesic acid on Cu(110). *J. Phys. Chem. A* **111**, 12589-12603 (2007).
28 Lin, N., Dmitriev, A., Weckesser, J., Barth, J. V. & Kern, K. Real-time single-molecule imaging of the formation and dynamics of coordination compounds. *Angew. Chem. Int. Ed. Engl.* **41**, 4779-4783 (2002).
29 Bartels, L. *et al.* Do Two-Dimensional "Noble Gas Atoms" Produce Molecular Honeycombs at a Metal Surface? *Nano Lett* **11**, 2944-2948 (2011).
30 Tseng, T. C. *et al.* Charge-transfer-induced structural rearrangements at both sides of organic/metal interfaces. *Nat Chem* **2**, 374-379 (2010).
31 Moore, A. M. & Weiss, P. S. Functional and Spectroscopic Measurements with Scanning Tunneling Microscopy. *Annu Rev Anal Chem* **1**, 857-882 (2008).
32 Chen, C. J. Introduction to scanning tunneling microscopy. *Oxford University Press* (1993).
33 Coombs, J. H., Welland, M. E. & Pethica, J. B. Experimental Barrier Heights and the Image Potential in Scanning Tunneling Microscopy. *Surf Sci* **198**, L353-L358 (1988).

34 Dunphy, J. C. *et al.* Acetylene structure and dynamics on Pd(111). *Phys Rev B* **57**, R12705-R12708 (1998).
35 Meyer, G., Bartels, L. & Rieder, K. H. Atom manipulation with the STM: nanostructuring, tip functionalization, and femtochemistry. *Comp Mater Sci* **20**, 443-450 (2001).
36 Hla, S. W., Kuhnle, A., Bartels, L., Meyer, G. & Rieder, K. H. Controlled lateral manipulation of single diiodobenzene molecules on the Cu(111) surface with the tip of a scanning tunnelling microscope. *Surf Sci* **454**, 1079-1084 (2000).
37 Meyer, G., Bartels, L., Zophel, S. & Rieder, K. H. Lateral manipulation of adatoms and native substrate atoms with the low-temperature scanning tunneling microscope. *Appl Phys a-Mater* **68**, 125-129 (1999).
38 Meyer, G., Bartels, L. & Rieder, K. H. Atom manipulation with the scanning tunneling microscope: Nanostructuring and femtochemistry. *Japanese Journal of Applied Physics Part 1-Regular Papers Short Notes & Review Papers* **37**, 7143-7147 (1998).
39 Bartels, L., Meyer, G. & Rieder, K. H. Atomic hop-scotch: different manipulation modes of single Cu atoms on Cu(111). *Chem Phys Lett* **285**, 284-287 (1998).
40 Bartels, L., Meyer, G. & Rieder, K. H. Basic steps of lateral manipulation of single atoms and diatomic clusters with a scanning tunneling microscope tip. *Phys Rev Lett* **79**, 697-700 (1997).
41 Hwang, I. S., Lo, R. L. & Tsong, T. T. Continuous-time observation of pseudo-vacancy diffusion at Si(111)-7x7 surfaces. *Surf Sci* **367**, L47-L53 (1996).
42 Hill, E., Freelon, B. & Ganz, E. Diffusion of hydrogen on the Si(001) surface investigated by STM atom tracking. *Phys Rev B* **60**, 15896-15900 (1999).
43 Rosso, K. M., Becker, U. & Hochella, M. F. Surface defects and self-diffusion on pyrite {100}: An ultra-high vacuum scanning tunneling microscopy and theoretical modeling study. *Am Mineral* **85**, 1428-1436 (2000).
44 Slezak, J., Chab, V., Chvoj, Z. & Mutombo, P. Study of Pb diffusion on Si(111)-(7x7) with scanning tunneling microscopy: Low coverage. *J Vac Sci Technol B* **18**, 1151-1155 (2000).
45 Wahl, M., von Arx, M., Jung, T. A. & Baiker, A. Time-lapse STM studies of diastereomeric cinchona alkaloids on platinum metals. *J Phys Chem B* **110**, 21777-21782 (2006).
46 Bartels, L. *et al.* Power of Confinement: Adsorbate Dynamics on Nanometer-Scale Exposed Facets. *Nano Lett* **10**, 3700-3703 (2010).
47 Buchner, F. *et al.* Diffusion, Rotation, and Surface Chemical Bond of Individual 2H-Tetraphenylporphyrin Molecules on Cu(111). *J Phys Chem C* **115**, 24172-24177 (2011).
48 Knorr, N., Schneider, M. A., Diekhoner, L., Wahl, P. & Kern, K. Kondo effect of single Co adatoms on Cu surfaces. *Phys Rev Lett* **88**, - (2002).

49 Chen, W., Madhavan, V., Jamneala, T. & Crommie, M. F. Scanning tunneling microscopy observation of an electronic superlattice at the surface of clean gold. *Phys Rev Lett* **80**, 1469-1472 (1998).
50 Malterre, D. *et al.* ARPES and STS investigation of Shockley states in thin metallic films and periodic nanostructures. *New J Phys* **9**, - (2007).
51 Didiot, C., Fagot-Revurat, Y., Pons, S., Kierren, B. & Malterre, D. ARPES and STS investigation of noble metal Shockley states: Confinement in vicinal Au(111) surfaces and self-organized nanostructures. *Surf Sci* **601**, 4029-4035 (2007).
52 Didiot, C., Vedeneev, A., Fagot-Revurat, Y., Kierren, B. & Malterre, D. Imaging a buried interface by scanning tunneling spectroscopy of surface states in a metallic system. *Phys Rev B* **72**, - (2005).
53 Liljeroth, P., Swart, I., Paavilainen, S., Repp, J. & Meyer, G. Single-Molecule Synthesis and Characterization of Metal-Ligand Complexes by Low-Temperature STM. *Nano Lett* **10**, 2475-2479 (2010).
54 Petukhov, K. *et al.* STM spectroscopy of magnetic molecules. *Coordin Chem Rev* **253**, 2387-2398 (2009).
55 Hla, S. W., Bartels, L., Meyer, G. & Rieder, K. H. Inducing all steps of a chemical reaction with the scanning tunneling microscope tip: Towards single molecule engineering. *Phys Rev Lett* **85**, 2777-2780 (2000).
56 Meyer, G., Bartels, L. & Rieder, K. H. Atom manipulation with the scanning tunneling microscope: nanostructuring and femtochemistry. *Superlattice Microst* **25**, 463-471 (1999).
57 Bartels, L. *et al.* Atomic-scale chemistry: Desorption of ammonia from Cu(111) induced by tunneling electrons. *Chem Phys Lett* **313**, 544-552 (1999).
58 Meyer, G., Bartels, L., Zophel, S., Henze, E. & Rieder, K. H. Controlled atom by atom restructuring of a metal surface with the scanning tunneling microscope. *Phys Rev Lett* **78**, 1512-1515 (1997).
59 Hla, S. W. Scanning tunneling microscope atom and molecule manipulations: Realizing molecular switches and devices. *Jpn J Appl Phys* **47**, 6063-6069 (2008).
60 Hla, S. W. Molecular machines - Reinventing the wheel. *Nat Nanotechnol* **2**, 82-84 (2007).
61 Hla, S. W. Scanning tunneling microscopy single atom/molecule manipulation and its application to nanoscience and technology. *J Vac Sci Technol B* **23**, 1351-1360 (2005).
62 Braun, K. F. & Hla, S. W. Probing the conformation of physisorbed molecules at the atomic scale using STM manipulation. *Nano Lett* **5**, 73-76 (2005).
63 Rieder, K. H. *et al.* The scanning tunnelling microscope as an operative tool: doing physics and chemistry with single atoms and molecules. *Philosophical Transactions of the Royal Society of London Series a-Mathematical Physical and Engineering Sciences* **362**, 1207-1216 (2004).

64 Hla, S. W., Braun, K. F., Wassermann, B. & Rieder, K. H. Controlled low-temperature molecular manipulation of sexiphenyl molecules on Ag(111) using scanning tunneling microscopy. *Phys Rev Lett* **93** (2004).
65 Hla, S. W. & Rieder, K. H. STM control of chemical reactions: Single-molecule synthesis. *Annu Rev Phys Chem* **54**, 307-330 (2003).
66 Hla, S. W., Braun, K. F. & Rieder, K. H. Single-atom manipulation mechanisms during a quantum corral construction. *Phys Rev B* **67** (2003).
67 Kuhnle, A., Meyer, G., Hla, S. W. & Rieder, K. H. Understanding atom movement during lateral manipulation with the STM tip using a simple simulation method. *Surf Sci* **499**, 15-23 (2002).
68 Hla, S. W. & Rieder, K. H. Engineering of single molecules with a scanning tunneling microscope tip. *Superlattice Microst* **31**, 63-72 (2002).
69 Moresco, F. *et al.* Manipulation of atoms, molecules and clusters for construction of nanosystems. *Chinese Phys* **10**, S10-S18 (2001).
70 Meyer, G. *et al.* Manipulation of atoms and molecules with the low-temperature scanning tunneling microscope. *Japanese Journal of Applied Physics Part 1-Regular Papers Short Notes & Review Papers* **40**, 4409-4413 (2001).
71 Hla, S. W., Meyer, G. & Rieder, K. H. Inducing single-molecule chemical reactions with a UHV-STM: A new dimension for nano-science and technology. *Chemphyschem* **2**, 361-366 (2001).
72 Bartels, L., Meyer, G. & Rieder, K. H. Lateral manipulation of single Cu atoms on flat and stepped copper surfaces. *J Vac Sci Technol A* **16**, 1047-1049 (1998).
73 Bartels, L. *et al.* Dynamics of electron-induced manipulation of individual CO molecules on Cu(III). *Phys Rev Lett* **80**, 2004-2007 (1998).
74 Bartels, L., Meyer, G. & Rieder, K. H. Basic steps involved in the lateral manipulation of single CO molecules and rows of CO molecules. *Chem Phys Lett* **273**, 371-375 (1997).
75 Bartels, L., Meyer, G. & Rieder, K. H. Controlled vertical manipulation of single CO molecules with the scanning tunneling microscope: A route to chemical contrast. *Appl Phys Lett* **71**, 213-215 (1997).
76 Haruta, M. Catalysis - Gold rush. *Nature* **437**, 1098-1099 (2005).
77 Heller, E., Crommie, M., Lutz, C. & Eigler, D. Scatterin and Adsorption of Surface Electron Waves in Quantum Corrals. *Nature* **369**, 464-466 (1994).
78 Rastei, M. V. *et al.* Size-dependent surface states of strained cobalt nanoislands on Cu(111). *Phys. Rev. Lett.* **99**, - (2007).
79 Gsell, M., Jakob, P. & Menzel, D. Effect of substrate strain on adsorption. *Science* **280**, 717-720 (1998).
80 Stranick, S. J., Kamna, M. M. & Weiss, P. S. Atomic-Scale Dynamics of a 2-Dimensional Gas-Solid Interface. *Science* **266**, 99-102 (1994).
81 Negulyaev, N. N. *et al.* Direct Evidence for the Effect of Quantum Confinement of Surface-State Electrons on Atomic Diffusion. *Phys. Rev. Lett.* **101**, - (2008).

82 Sykes, E. *et al.* Substrate-mediated interactions and intermolecular forces between molecules adsorbed on surfaces. *Acc. Chem. Res.* **36**, 945-953 (2003).
83 Nanayakkara, S. U., Sykes, E. C. H., Fernandez-Torres, L. C., Blake, M. M. & Weiss, P. S. Long-Range Electronic Interactions at a High Temperature: Bromine Adatom Islands on Cu(111). *Phys. Rev. Lett.* **98**, 206108-206104 (2007).
84 Lukas, S., Witte, G. & Woll, C. Novel mechanism for molecular self-assembly on metal substrates: Unidirectional rows of pentacene on Cu(110) produced by a substrate-mediated repulsion. *Phys. Rev. Lett.* **88**, 028301 (2002).
85 Wong, K. L., Rao, B. V., Pawin, G., Ulin-Avila, E. & Bartels, L. Coverage and nearest-neighbor dependence of adsorbate diffusion. *J. Chem. Phys.* **123**, 201102 (2005).
86 Mitsui, T., Rose, M. K., Fomin, E., Ogletree, D. F. & Salmeron, M. Diffusion and pair interactions of CO molecules on Pd(111). *Phys. Rev. Lett.* **94**, 036101 (2005).
87 Repp, J. *et al.* Substrate mediated long-range oscillatory interaction between adatoms: Cu/Cu(111). *Phys. Rev. Lett.* **85**, 2981-2984 (2000).
88 Einstein, T. L. in *Physical structure of solid surfaces, Handbook of surface science ; v. 1* (ed W. N. Unertl) Ch. Interactions between Adsorbate Particles, 577-650 (Elsevier, 1996).
89 Fichthorn, K. & Scheffler, M. Island nucleation in thin-film epitaxy: A first-principles investigation. *Phys. Rev. Lett.* **84**, 5371-5374 (2000).
90 Österlund, L., Pedersen, M., Stensgaard, I., Laesgaard, E. & Besenbacher, F. Quantitative determination of adsorbate-adsorbate interactions. *Phys. Rev. Lett.* **83**, 4812-4815 (1999).
91 Stepanyuk, V. *et al.* Quantum interference and long-range adsorbate-adsorbate interactions. *Phys. Rev. B* **68**, - (2003).
92 Kulawik, M. *et al.* Interaction of CO molecules with surface state electrons on Ag(111). *Surf. Sci.* **590**, L253-L258 (2005).
93 Hyldgaard, P. & Einstein, T. L. Surface-state mediated three-adsorbate interaction. *Europhys. Lett.* **59**, 265-271 (2002).
94 Bogicevic, A. *et al.* Nature, strength, and consequences of indirect adsorbate interactions on metals. *Phys. Rev. Lett.* **85**, 1910-1913 (2000).
95 Bartels, L., Meyer, G. & Rieder, K. Controlled vertical manipulation of single CO molecules with the scanning tunneling microscope: A route to chemical contrast. *Appl. Phys. Lett.* **71**, 213-215 (1997).
96 Mathews, J. & Walker, R. L. *Mathematical methods of physics*. 2d edn, (W. A. Benjamin, 1970).
97 Gross, L. *et al.* Scattering of surface state electrons at large organic molecules. *Phys. Rev. Lett.* **93**, 056103 (2004).
98 Atkinson, K. E. & Han, W. *Elementary numerical analysis*. 3rd edn, (J. Wiley & Sons, 2004).

99 Kiełbasiński, A. & Schwetlick, H. *Numerische lineare Algebra : eine computerorientierte Einführung*. (Harri Deutsch, 1988).
100 Fiete, G. A. & Heller, E. J. Colloquium: Theory of quantum corrals and quantum mirages. *Rev. Mod. Phys.* **75**, 933-948 (2003).
101 Kevan, S. D. & Gaylord, R. H. High-Resolution Photoemission-Study of the Electronic-Structure of the Noble-Metal (111) Surfaces. *Phys. Rev. B* **36**, 5809-5818 (1987).
102 Burgi, L., Petersen, L., Brune, H. & Kern, K. Noble metal surface states: deviations from parabolic dispersion. *Surf. Sci.* **447**, L157-L161 (2000).
103 Haruta, M., Kobayashi, T., Sano, H. & Yamada, N. Novel Gold Catalysts for the Oxidation of Carbon-Monoxide at a Temperature Far Below 0-Degrees-C. *Chemistry Letters*, 405-408 (1987).
104 Chen, M. S. & Goodman, D. W. The structure of catalytically active gold on titania. *Science* **306**, 252-255 (2004).
105 Somorjai, G. A. *Introduction to surface chemistry and catalysis*. (Wiley, 1994).
106 Mantooth, B. A. *et al.* Analyzing the motion of benzene on Au{111}: Single molecule statistics from scanning probe images. *J. Phys. Chem. C* **111**, 6167-6182 (2007).
107 Han, P., Mantooth, B., Sykes, E., Donhauser, Z. & Weiss, P. Benzene on Au (111) at 4 K: Monolayer growth and tip-induced molecular cascades. *J. Am. Chem. Soc.* **126**, 10787-10793 (2004).
108 Sachs, C., Hildebrand, M., Volkening, S., Wintterlin, J. & Ertl, G. Spatiotemporal self-organization in a surface reaction: From the atomic to the mesoscopic scale. *Science* **293**, 1635-1638 (2001).
109 Hendriksen, B., Bobaru, S. & Frenken, J. Oscillatory CO oxidation on Pd(100) studied with in situ scanning tunneling microscopy. *Surf. Sci.* **552**, 229-242 (2004).
110 Tierney, H. L., Baber, A. E. & Sykes, E. C. H. Atomic-Scale Imaging and Electronic Structure Determination of Catalytic Sites on Pd/Cu Near Surface Alloys. *J. Phys. Chem. C* **113**, 7246-7250 (2009).
111 Briner, B., Doering, M., Rust, H. & Bradshaw, A. Microscopic molecular diffusion enhanced by adsorbate interactions. *Science* **278**, 257-260 (1997).
112 Heinrich, A., Lutz, C., Gupta, J. & Eigler, D. Molecule cascades. *Science* **298**, 1381-1387 (2002).
113 Longwitz, S. *et al.* High-coverage structures of carbon monoxide adsorbed on Pt(111) studied by high-pressure scanning tunneling microscopy. *J. Phys. Chem. B* **108**, 14497-14502 (2004).
114 Stepanow, S. *et al.* Steering molecular organization and host-guest interactions using two-dimensional nanoporous coordination systems. *Nat. Mater.* **3**, 229-233 (2004).
115 Decker, R. *et al.* Using metal-organic templates to steer the growth of Fe and Co nanoclusters. *Appl. Phys. Lett.* **93**, 243102 (2008).

116 Berner, S. *et al.* Boron nitride nanomesh: Functionality from a corrugated monolayer. *Angew. Chem. Int. Ed. Engl.* **46**, 5115-5119 (2007).
117 Otero, R. *et al.* Nanostructuring Cu surfaces using custom-designed molecular molds. *Nano Lett* **4**, 75-78 (2004).
118 Static Confinement of CO in much larger edge-pits has been investigated by Kulawik et al., Surf. Sci. 590, L53 (2005)
119 Bartels, L., Meyer, G. & Rieder, K. The evolution of CO adsorption on Cu(111) as studied with bare and CO-functionalized scanning tunneling tips. *Surf. Sci.* **432**, L621-L626 (1999).
120 Shan, B. *et al.* Coverage-Dependent CO Adsorption Energy from First-Principles Calculations. *J. Phys. Chem. C* **113**, 6088-6092 (2009).
121 Elemans, J. A. A. W., Lei, S. B. & De Feyter, S. Molecular and Supramolecular Networks on Surfaces: From Two-Dimensional Crystal Engineering to Reactivity. *Angew. Chem. Int. Ed. Engl.* **48**, 7298-7332 (2009).
122 Schickum, U. *et al.* Metal-organic honeycomb nanomeshes with tunable cavity size. *Nano Lett* **7**, 3813-3817 (2007).
123 Kuhne, D. *et al.* High-Quality 2D Metal-Organic Coordination Network Providing Giant Cavities within Mesoscale Domains. *J. Am. Chem. Soc.* **131**, 3881 (2009).
124 Schlickum, U. *et al.* Chiral kagome lattice from simple ditopic molecular bricks. *J. Am. Chem. Soc.* **130**, 11778-11782 (2008).
125 Kwon, K. Y. *et al.* H-Atom Position as Pattern-Determining Factor in Arenethiol Films. *J. Am. Chem. Soc.* **131**, 5540-5545 (2009).
126 Tait, S. L. *et al.* Assembling Isostructural Metal-Organic Coordination Architectures on Cu(100), Ag(100) and Ag(111) Substrates. *Chem. Phys. Chem.* **9**, 2495-2499 (2008).
127 Pawin, G. *et al.* A Surface Coordination Network Based on Substrate-Derived Metal Adatoms with Local Charge Excess. *Angew Chem Int Edit* **47**, 8442-8445 (2008).
128 Grill, L. *et al.* Nano-architectures by covalent assembly of molecular building blocks. *Nat. Nanotechnol.* **2**, 687-691 (2007).
129 Lipton-Duffin, J. A., Ivasenko, O., Perepichka, D. F. & Rosei, F. Synthesis of Polyphenylene Molecular Wires by Surface-Confined Polymerization. *Small* **5**, 592-597 (2009).
130 Matena, M., Riehm, T., Stohr, M., Jung, T. A. & Gade, L. H. Transforming surface coordination polymers into covalent surface polymers: Linked polycondensed aromatics through oligomerization of N-heterocyclic carbene intermediates. *Angew. Chem.-Int. Edit.* **47**, 2414-2417 (2008).
131 Hla, S., Bartels, L., Meyer, G. & Rieder, K. Inducing all steps of a chemical reaction with the scanning tunneling microscope tip: Towards single molecule engineering. *Phys. Rev. Lett.* **85**, 2777-2780 (2000).

132 Veld, M. I., Iavicoli, P., Haq, S., Amabilino, D. B. & Raval, R. Unique intermolecular reaction of simple porphyrins at a metal surface gives covalent nanostructures. *Chem. Com.*, 1536-1538 (2008).
133 Sykes, E. C. H. *et al.* Substrate-mediated interactions and intermolecular forces between molecules adsorbed on surfaces. *Accounts Chem. Res.* **36**, 945-953 (2003).
134 Knorr, N. *et al.* Long-range adsorbate interactions mediated by a two-dimensional electron gas. *Phys. Rev, B, Condens, Matter Mater. Phys.* **65**, 115420/115421-115420/115425 (2002).
135 Silly, F. *et al.* Creation of an atomic superlattice by immersing metallic adatoms in a two-dimensional electron sea. *Phys. Rev. Lett.* **92**, 016101 (2004).
136 Wang, Y. F. *et al.* Supramolecular Patterns Controlled by Electron Interference and Direct Intermolecular Interactions. *J. Am. Chem. Soc.* **131**, 10400-+ (2009).
137 Mehlhorn, M., Simic-Milosevic, V., Jaksch, S., Scheier, P. & Morgenstern, K. The influence of the surface state onto the distance distribution of single molecules and small molecular clusters. *Surf Sci* **604**, 1698-1704 (2010).
138 Sohn, Y., Wei, W. & White, J. M. 1-phenyl-1-propyne on Cu(111): TOFMS TPD, XPS, UPS, and 2PPE studies. *Langmuir* **23**, 12185-12191 (2007).
139 Sohn, Y., Wei, W. & White, J. M. Phenylacetylene on Cu(111): Adsorption geometry, interfacial electronic structures and thermal chemistry. *J. Phys. Chem. C* **111**, 5101-5110 (2007).
140 Kuhne, D. *et al.* Self-Assembly of Nanoporous Chiral Networks with Varying Symmetry from Sexiphenyl-dicarbonitrile on Ag(111). *J. Phys. Chem. C* **113**, 17851-17859 (2009).
141 Jeffrey, G. A. *An Introduction to Hydrogen Bonding*. (Oxford University Press, Oxford, 1997).
142 Kresse, G. & Hafner, J. Abinitio Molecular-Dynamics for Liquid-Metals. *Phys. Rev. B* **47**, 558-561 (1993).
143 Perdew, J. P. & Wang, Y. Accurate and Simple Analytic Representation of the Electron-Gas Correlation-Energy. *Phys. Rev. B* **45**, 13244-13249 (1992).
144 Payne, M. C., Teter, M. P., Allan, D. C., Arias, T. A. & Joannopoulos, J. D. Iterative Minimization Techniques for Abinitio Total-Energy Calculations - Molecular-Dynamics and Conjugate Gradients. *Rev. Mod. Phys.* **64**, 1045-1097 (1992).
145 Vanderbilt, D. Soft Self-Consistent Pseudopotentials in a Generalized Eigenvalue Formalism. *Phys. Rev. B* **41**, 7892-7895 (1990).
146 Blum, M. C., Cavar, E., Pivetta, M., Patthey, F. & Schneider, W. D. Conservation of chirality in a hierarchical supramolecular self-assembled structure with pentagonal symmetry. *Angew. Chem.-Int. Edit.* **44**, 5334-5337 (2005).
147 Ye, Y. C. *et al.* A unified model: Self-assembly of trimesic acid on gold. *J. Phys. Chem. C* **111**, 10138-10141 (2007).

148 Coratger, R., Calmettes, B., Abel, M. & Porte, L. STM observations of the first polymerization steps between hexahydroxy-tri-phenylene and benzene-di-boronic acid molecules. *Surf Sci* **605**, 831-837 (2011).
149 Kwon, K. Y. *et al.* Unidirectional adsorbate motion on a high-symmetry surface: "Walking" molecules can stay the course. *Phys. Rev. Lett.* **95**, 166101 (2005).
150 Cheng, Z. *et al.* Tunability in Polyatomic Molecule Diffusion through Tunneling versus Pacing. *J. Am. Chem. Soc.* **132**, 13578 (2010).
151 Wong, K. L. *et al.* A Molecule Carrier. *Science* **315**, 1391-1393 (2007).
152 Berland, K., Einstein, T. L. & Hyldgaard, P. Rings sliding on a honeycomb network: Adsorption contours, interactions,and assembly of benzene on Cu(111). *Phys. Rev. B* **80**, 155431 (2009).
153 Sun, D. Z. *et al.* Effective elastic properties of a van der Waals molecular monolayer at a metal surface. *Phys. Rev. B* **82**, 201410 (2010).
154 Bilic, A., Reimers, J. R., Hush, N. S., Hoft, R. C. & Ford, M. J. Adsorption of benzene on copper, silver, and gold surfaces. *J. Chem. Theory Comput.* **2**, 1093-1105 (2006).
155 Dion, M., Rydberg, H., Schröder, E., Langreth, D. C. & Lundqvist, B. I. Van der Waals density functional for general geometries. *Phys. Rev. Lett.* **92**, 246401 (2004).
156 Koch, N. *et al.* Adsorption-induced intramolecular dipole: Correlating molecular conformation and interface electronic structure. *J. Am. Chem. Soc.* **130**, 7300-7304 (2008).
157 Wong, K., Kwon, K., Rao, B., Liu, A. & Bartels, L. Effect of halo substitution on the geometry of arenethiol films on Cu(111). *J. Am. Chem. Soc.* **126**, 7762-7763 (2004).
158 Yaghi, O. M. *et al.* Reticular synthesis and the design of new materials. *Nature* **423**, 705-714 (2003).
159 Ruben, M., Rojo, J., Romero-Salguero, F. J., Uppadine, L. H. & Lehn, J. M. Grid-type metal ion architectures: Functional metallosupramolecular arrays. *Angew. Chem. Int. Ed. Engl.* **43**, 3644-3662 (2004).
160 Dmitriev, A., Spillmann, H., Lin, N., Barth, J. V. & Kern, K. Modular assembly of two-dimensional metal-organic coordination networks at a metal surface. *Angew Chem Int Edit* **42**, 2670-2673 (2003).
161 Barth, J. V., Costantini, G. & Kern, K. Engineering atomic and molecular nanostructures at surfaces. *Nature* **437**, 671-679 (2005).
162 Zhu, N., Osada, T. & Komeda, T. Supramolecular assembly of biphenyl dicarboxylic acid on Au(1 1 1). *Surf. Sci.* **601**, 1789-1794 (2007).
163 Tait, S. L. *et al.* Metal-organic coordination interactions in Fe-Terephthalic acid networks on Cu(100). *J. Am. Chem. Soc.* **130**, 2108-2113 (2008).
164 Breitruck, A., Hoster, H. E., Meier, C., Ziener, U. & Behm, R. J. Interaction of Cu atoms with ordered 2D oligopyridine networks. *Surf. Sci.* **601**, 4200-4205 (2007).

165 Zhang, H. M. *et al.* One-step preparation of large-scale self-assembled monolayers of cyanuric acid and melamine supramolecular species on Au(111) surfaces. *J. Phys. Chem. C* **112**, 4209-4218 (2008).
166 Surin, M., Samori, P., Jouaiti, A., Kyritsakas, N. & Hosseini, M. W. Molecular tectonics on surfaces: Bottom-up fabrication of 1D coordination networks that form 1D and 2D arrays on graphite. *Angew. Chem. Int. Ed. Engl.* **46**, 245-249 (2007).
167 Walch, H. *et al.* Extended Two-Dimensional Metal-Organic Frameworks Based on Thiolate-Copper Coordination Bonds. *J Am Chem Soc* **133**, 7909-7915 (2011).
168 Voznyy, O., Dubowski, J. J., Yates, J. T. & Maksymovych, P. The Role of Gold Adatoms and Stereochemistry in Self-Assembly of Methylthiolate on Au(111). *J Am Chem Soc* **131**, 12989-12993 (2009).
169 Maksymovych, P., Sorescu, D. C. & Yates, J. T. Gold-adatom-mediated bonding in self-assembled short-chain alkanethiolate species on the Au(111) surface. *Phys Rev Lett* **97**, - (2006).
170 Maksymovych, P. & Yates, J. T. Au adatoms in self-assembly of benzenethiol on the Au(111) surface. *J Am Chem Soc* **130**, 7518-+ (2008).
171 Wang, W. H. *et al.* Inspecting Metal-Coordination-Induced Perturbation of Molecular Ligand Orbitals at a Submolecular Resolution. *J Phys Chem Lett* **1**, 2295-2298 (2010).
172 Shi, Z. L. & Lin, N. Self-Assembly of a Two-Dimensional Bimetallic Coordination Framework and Dynamic Control of Reversible Conversions to Homo-Metallic Hydrogen-Bond Arrays. *Chemphyschem* **11**, 97-100 (2010).
173 Shi, Z. L. & Lin, N. Structural and Chemical Control in Assembly of Multicomponent Metal-Organic Coordination Networks on a Surface. *J Am Chem Soc* **132**, 10756-10761 (2010).
174 Heim, D. *et al.* Surface-Assisted Assembly of Discrete Porphyrin-Based Cyclic Supramolecules. *Nano Lett* **10**, 122-128 (2010).
175 Heim, D. *et al.* Self-Assembly of Flexible One-Dimensional Coordination Polymers on Metal Surfaces. *J Am Chem Soc* **132**, 6783-6790 (2010).
176 Langner, A. *et al.* Two- to one-dimensional transition of self-assembled coordination networks at surfaces by organic ligand addition. *Chem Commun*, 2502-2504 (2009).
177 Langner, A. *et al.* Ordering and Stabilization of Metal-Organic Coordination Chains by Hierarchical Assembly through Hydrogen Bonding at a Surface. *Angew. Chem. Int. Ed. Engl.* **47**, 8835-8838 (2008).
178 Lin, N., Stepanow, S., Vidal, F., Barth, J. V. & Kern, K. Manipulating 2D metal-organic networks via ligand control. *Chem Commun*, 1681-1683 (2005).
179 Canas-Ventura, M. E. *et al.* Complex Interplay and Hierarchy of Interactions in Two-Dimensional Supramolecular Assemblies. *Acs Nano* **5**, 457-469 (2011).
180 Tseng, T. C., Abdurakhmanova, N., Stepanow, S. & Kern, K. Hierarchical Assembly and Reticulation of Two-Dimensional Mn- and Ni-TCNQ(x) (x=1,

2,4) Coordination Structures on a Metal Surface. *J Phys Chem C* **115**, 10211-10217 (2011).
181 Henningsen, N. *et al.* Site-Dependent Coordination Bonding in Self-Assembled Metal-Organic Networks. *J Phys Chem Lett* **2**, 55-61 (2011).
182 Marschall, M. *et al.* Random two-dimensional string networks based on divergent coordination assembly. *Nat Chem* **2**, 131-137 (2010).
183 Fendt, L. A. *et al.* Modification of Supramolecular Binding Motifs Induced By Substrate Registry: Formation of Self-Assembled Macrocycles and Chain-Like Patterns. *Chem-Eur J* **15**, 11139-11150 (2009).
184 Tseng, T. C. *et al.* Two-dimensional metal-organic coordination networks of Mn-7,7,8,8-tetracyanoquinodimethane assembled on Cu(100): Structural, electronic, and magnetic properties. *Phys Rev B* **80**, - (2009).
185 Boscoboinik, J. A. *et al.* One-dimensional supramolecular surface structures: 1,4-diisocyanobenzene on Au(111) surfaces. *Phys Chem Chem Phys* **12**, 11624-11629 (2010).
186 Zhang, Y. F., Zhu, N. & Komeda, T. Programming of a Mn-coordinated 4-4 '-biphenyl dicarboxylic acid nanosystem on Au(111) and investigation of the non-covalent binding of C60 molecules. *Surf Sci* **602**, 614-619 (2008).
187 Zhang, Y. F., Zhu, N. & Komeda, T. Mn-coordinated stillbenedicarboxylic ligand supramolecule regulated by the herringbone reconstruction of Au(111). *J Phys Chem C* **111**, 16946-16950 (2007).
188 Lin, N. *et al.* Surface-assisted coordination chemistry and self-assembly. *Dalton T*, 2794-2800 (2006).
189 Dougherty, D. B., Maksymovych, P. & Yates, J. T. Direct STM evidence for Cu-benzoate surface complexes on Cu(110). *Surf Sci* **600**, 4484-4491 (2006).
190 Lingenfelder, M. A. *et al.* Towards surface-supported supramolecular architectures: tailored coordination assembly of 1,4-benzenedicarboxylate and Fe on Cu(100). *Chem-Eur J* **10**, 1913-1919 (2004).
191 Spillmann, H. *et al.* Hierarchical assembly of two-dimensional homochiral nanocavity arrays. *J Am Chem Soc* **125**, 10725-10728 (2003).
192 Barth, J. V., Weckesser, J., Lin, N., Dmitriev, A. & Kern, K. Supramolecular architectures and nanostructures at metal surfaces. *Appl Phys a-Mater* **76**, 645-652 (2003).
193 Jensen, S. & Baddeley, C. J. Formation of PTCDI-based metal organic structures on a Au(111) surface modified by 2-D Ni clusters. *J Phys Chem C* **112**, 15439-15448 (2008).
194 Matena, M. *et al.* Aggregation and Contingent Metal/Surface Reactivity of 1,3,8,10-Tetraazaperopyrene (TAPP) on Cu(111). *Chem-Eur J* **16**, 2079-2091 (2010).
195 Walch, H., Gutzler, R., Sirtl, T., Eder, G. & Lackinger, M. Material- and Orientation-Dependent Reactivity for Heterogeneously Catalyzed Carbon-Bromine Bond Homolysis. *J Phys Chem C* **114**, 12604-12609 (2010).

196 Schiffrin, A. *et al.* Self-aligning atomic strings in surface-supported biomolecular gratings. *Phys. Rev. B* **78**, 035424 (2008).
197 Greenwood, N. N. & Earnshaw, A. xxii, 1341 p. (Butterworth-Heinemann, Oxford ; Boston, 1998).